Nanoscale

ROYAL SOCIETY OF CHEMISTRY

PAPER

View Article Online
View Journal | View Issue

Cite this: *Nanoscale*, 2025, **17**, 5907

Rare earth orthovanadate (REM-VO_4; REM = Pr, Gd, and Sm)-based sensors for selective and simultaneous detection of furazolidone and metronidazole†

Pandiyan Bharathi and Sea-Fue Wang *

Antibiotics are vital tools in the fight against bacterial infections, with furazolidone (FD) and metronidazole (MD) being widely used to target pathogens like *G. lamblia* and *H. pylori*. However, overuse of these antibiotics can lead to serious health complications, highlighting the urgent need for accurate, real-time detection of these drugs at precise levels. In this study, we explore the use of differential pulse voltammetry (DPV) for detecting FD and MD with high sensitivity, employing a dual detection method. To enhance detection, we developed a sensor using rare earth metal-based orthovanadates (REM-VO_4, where REM = Pr, Gd, and Sm) as electrode modifiers. These materials offer exceptional surface control, boosting the sensor's sensitivity and selectivity. Among the different configurations, the $SmVO_4$-modified glassy carbon electrode (SmV/GCE) stands out, demonstrating the lowest charge transfer resistance (R_{ct} = 56.82 Ω) and the largest electrochemical surface area (A = 0.11 cm^2). $SmVO_4$'s unique nanostructure, with its high electrochemically active surface area and hollow structure, is key to its impressive performance. This sensor not only provides the lowest limits of detection (0.0009 μM for FD and 0.0036 μM for MD individually, and 0.0015 μM and 0.0049 μM for simultaneous detection) but also shows excellent anti-interference, repeatability, and reproducibility. Furthermore, SmV/GCE has been successfully applied for real-time analysis of biological and environmental samples, offering recoveries between 97.33 to 99.60%, demonstrating its practical potential for precise antibiotic monitoring.

Received 4th November 2024,
Accepted 14th December 2024

DOI: 10.1039/d4nr04594g

rsc.li/nanoscale

1. Introduction

Since the beginning of evolution, the impact of infectious diseases on human society has been an unavoidable obstacle in many ways. Plague, influenza, malaria from the past to present, and COVID are a few examples of this. Giardia is one of the bacterial infections that was initially discovered by van Leeuwenhoek in 1681 and later renamed as *G. lamblia* in 1915 by Christiansen and Kofoid.[1,2] The infection caused by *G. lamblia* results in weight loss and chronic or acute diarrhea.[3,4] Similarly, *Helicobacter pylori* is another kind of bacterial infection usually found in the human stomach.[5] *H. pylori* can cause duodenal ulcers.[6] These diseases are globally spread infections and can be found at the end of pre-adolescence.[7] Antibodies are one of the revolutionary findings that act as a solution for these diseases.[8] Furazolidone (FD) and metronidazole (MD) are the antibiotics used to treat *G. lamblia* and *H. pylori*.[9,10] FD (3-(5-nitrofurfurylideneamino)-2-oxazolidinone) and MD (1-(2-hydroxyethyl)-2-methyl-5-nitroimidazole) are nitro-functional synthetic drugs that have been used for over 30 years as antibiotics.[11,12] FD and MD can also act as antibacterial and antiprotozoal agents for shrimp, cattle, poultry, and fish; thus, considerable quantities are added to their foodstuffs.[13] The cumulative allowed concentration values of FD and MD are 5 ng g^{-1} and 2 g, respectively.[14,15] Due to the low cost of FD, the developing countries are using it to treat *H. pylori* and the extermination rate is 75.7% to 79.6%.[16] FD is a good alternative for MD in *H. pylori* treatment.[9] Similarly, to treat *G. lamblia*, about 0.2 g of MD is used three times per day.[17] Also, the use of FD and MD causes some side effects, therefore some developed countries have banned them. The use of FD rarely leads to pulmonary hypersensitivity during the *H. pylori* treatment. Sometimes, FD is harmful to human DNA and stops cell growth in the S phase.[15] Apart from the excess use of FD and MD, it causes some common side effects such as diarrhea, fever, nausea, and rash.[18] On the other hand the global distribution of pharmaceuticals is increasing due to their widespread availability and the difficulty in their proper disposal. Also, animal farms are a sig-

Department of Materials and Mineral Resources Engineering, National Taipei University of Technology, Taipei 106, Taiwan. E-mail: sfwang@ntut.edu.tw

† Electronic supplementary information (ESI) available. See DOI: https://doi.org/10.1039/d4nr04594g

nificant source of pharmaceutical contamination in the environment mostly due to the use of antibiotics as feed additives. These medications enter the environment *via* sewage systems or underground water from waste disposal sites. The discharge of these compounds into terrestrial and aquatic environments without any form of control might result in the contamination of the environmental system.[19] So, quantifying FD and MD is essential in animal-based products and environmental samples. High-performance liquid chromatography, fluorimetry, liquid chromatography-mass spectrometry, capillary zone electrophoresis, and the use of electrochemical sensors are the few existing techniques used to determine FD and MD.[20,21] Expensive instrumentation, sample pre-treatment, and long experimental duration make them less convenient than the electrochemical sensing method. Since the use of electrochemical sensors is one of the sustainable methods that overcome these issues because it is cost-effective, simple, and easy to implement, it is considered a simple technique for the simultaneous detection of FD and MD.[22,23]

Electrochemical sensors function based on the signal produced by the electrochemical reaction (the interaction between the electrode and analyte). CV, DPV, LSV, and *i–t* are the most used techniques in electrochemical sensors.[24,25] Though *i–t* is more sensitive than other techniques, it cannot be used for simultaneous detection of analytes. The non-faradaic and faradaic current decay rates differentiate the DPV as the more sensitive technique than the CV and LSV. Even with the lower current response from the analyte, the DPV can differentiate the faradaic current rate from the non-faradaic current rate, making this a sensitive technique that is also beneficial for the simultaneous detection of analytes.[26] Moving to the working electrode, the glassy carbon electrodes (GCEs) are highly conductive, chemically stable, reusable, and easy to use for surface modification, which is favorable for the electrochemical sensors. However, obtaining a low detection limit is difficult due to the lack of active sites or low active surface area.[27] Surface modification of the GCE is one of the ways to overcome this issue.[28,29] Metal oxides, metal sulfides, double-layered hydroxides, and carbon-based materials are a few examples of surface modifiers.[30–32]

Nanomaterial-based electrode modifiers provide a large electrochemical surface area due to their smaller particle size, strong adsorption capacity, and superficial surface modification. This enables the integration between the target analyte and electrode modifiers and increases electron transportation.[33,34] Moreover, the amalgamation of nanomaterials/nanotechnology in the electrochemical sensor leads to enhanced catalytic behavior, precise analyte detection, and improved stability. Carbon-based nanomaterials such as nanographene and graphene oxide, noble metals like gold (Au), platinum (Pt), and silver (Ag)-based nanoparticles, and potential metal oxides are very few examples that are utilized in electrochemical sensors and biosensors.[35] Metal oxides have advantages such as high surface area, chemical stability, good sensitivity, and electron transportation, which promote the use of metal oxides in electrochemical sensors.[36,37] Due to their nanoscale dimensions and structural characteristics, the rapid electron transfer between the transducer and analyte molecule in the presence of metal nanoparticles designates them as electrocatalysts and electronic wires.[38,39]

Among the metal oxides, rare earth metal-based orthovanadates (REM-VO_4) (REM = La, Ce, ⋯) have arisen as a good electrode modifier in recent days because of their good ionic conductivity, appreciable band gaps, and low charge transfer resistance.[40–42] The perfect charge distribution between the Ln^{3+} (Ln – lanthanides) and $[VO_4]^{3-}$ tetrahedral oxyanions is also helpful in boosting the physicochemical properties of the material.[43] The abovementioned properties enable the implementation of REM-VO_4 in various applications such as energy storage, catalysis, optical devices, and sensors.[44] The presence of 4f orbitals in REM-VO_4 enables the variant electronic transition states to have better sensing properties.[45] Tetragonal zircon and monoclinic monazite are two basic polymorphs of REM-VO_4. From this, the zircon-type materials have been paid more attention, and they play a significant role as electrocatalysts, photocatalysts, and optical devices.[46] In the field of electrochemical sensors, it is evident that REM-VO_4-based materials are used as suitable electrode modifiers toward the lower detection limit. Moreover, REM-VO_4 can act as an excellent electrochemical catalyst for detecting nitro-functional analytes.[47] Our group has carried out a comparison of tetragonal REM-VO_4-based materials for the detection of nitro-functional analytes. For example, B. Sriram *et al.* used REM-VO_4 (REM = Ho, Y, and Dy) as electrode modifiers for detecting nitrofurazone and roxarsone.[48] Similarly, A. Radha *et al.* performed the electrochemical detection of metronidazole using REM-VO_4 (REM = Ce, Pr, or Nd) as electrode modifiers.[49] Further in this work, we chose a zircon-type tetragonal crystal structured REM-VO_4 (REM = Pr, Gd, or Sm) as an electrochemical tool for the detection of FD and MD. Hydrothermal synthesis is one of the effective ways to synthesize materials with uniform morphology, good crystalline nature, low temperature processing, and good purity.[50]

To the best of our knowledge, this is the first work reporting the comparison of REM-VO_4 (REM = Pr, Gd, and Sm) as an electrode modifier for the simultaneous detection of FD and MD. The targeted $PrVO_4$, $GdVO_4$, and $SmVO_4$ are synthesized *via* a hydrothermal method. The as-synthesized materials are characterized by various phase composition and morphological analysis techniques. EIS, CV, and DPV are used for the electrochemical evaluation of the as-synthesized materials. The result shows an excellent linear range, low detection limit, and good recovery range toward FD and MD. A schematic representation of the conceptual framework of the study is given in Scheme 1

2. Experimental details

2.1. Materials

Praseodymium(III) nitrate hexahydrate-99.9% ($Pr(NO_3)_3{\cdot}6H_2O$), gadolinium(III) nitrate hexahydrate-99.99% ($Gd(NO_3)_3{\cdot}6H_2O$), samarium(III) nitrate hexahydrate-99.9% ($Sm(NO_3)_3{\cdot}6H_2O$), ammonium metavanadate-99.0% (NH_4VO_3), urea-99.0% (CO

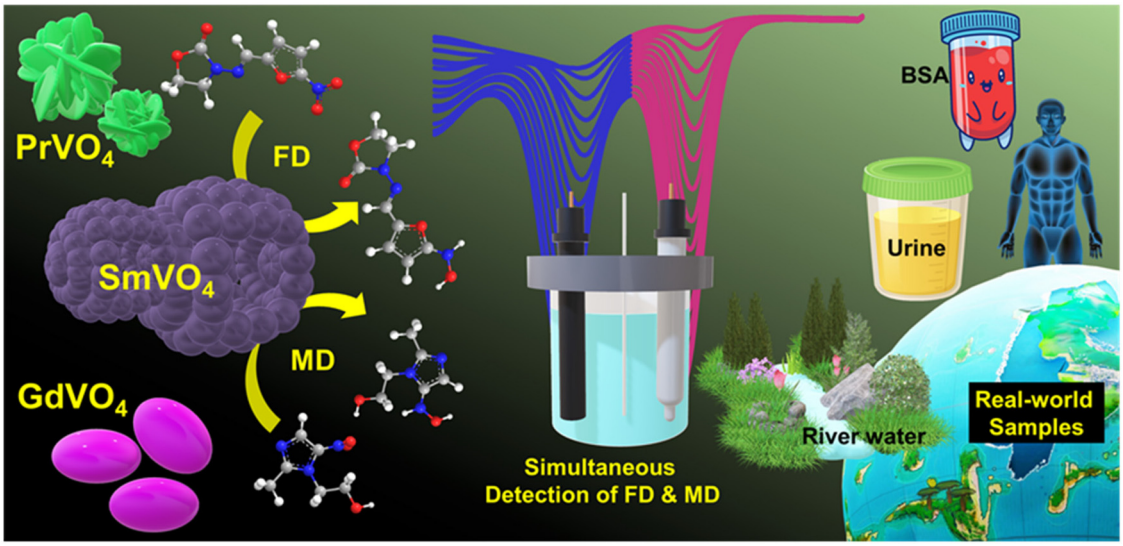

Scheme 1 Schematic representation of the conceptual framework of the study.

$(NH_2)_2$), bovine serum albumin-98.5% (BSA), furazolidone-98.0% ($C_8H_7N_3O_5$), and metronidazole-99.0% ($C_6H_9N_3O_3$) were purchased from Sigma-Aldrich. All the purchased chemicals were used directly without any purification process.

2.2. Synthesis of REM-VO_4 (REM = Pr, Gd, and Sm)

Solution A was prepared using 0.1 M ($Pr(NO_3)_3{\cdot}6H_2O$) dissolved in 75 mL of DI water. Then, solution B was prepared with 0.2 M NH_4VO_3 and 0.5 g of urea dissolved in 75 mL of DI water. When solution B became homogeneous, solution A was added drop by drop into solution B, followed by stirring for 60 min. The obtained solution was transferred into 200 mL of Teflon-lined autoclave, and the hydrothermal reaction was carried out at 180 °C for 12 h. When the temperature reached room temperature, the obtained residue was washed/centrifuged with DI water and ethanol. Finally, the residue was dried at 60 °C and crushed into fine powder. The sample is denoted as $PrVO_4$. Similarly, the same experimental conditions were used to synthesize $GdVO_4$ and $SmVO_4$, except solution A was prepared by their respective nitrate sources ($Gd(NO_3)_3{\cdot}6H_2O$ and Sm $(NO_3)_3{\cdot}6H_2O$). A schematic representation of the synthesis method is given in Scheme 2.

2.3. Surface modification GCE with REM-VO_4 (REM = Pr, Gd, and Sm)

Initially, the active surface area of the GCE was polished well with alumina slurry (0.05 μM). After washing with DI water, a continuous cycle was performed in the neutral medium of

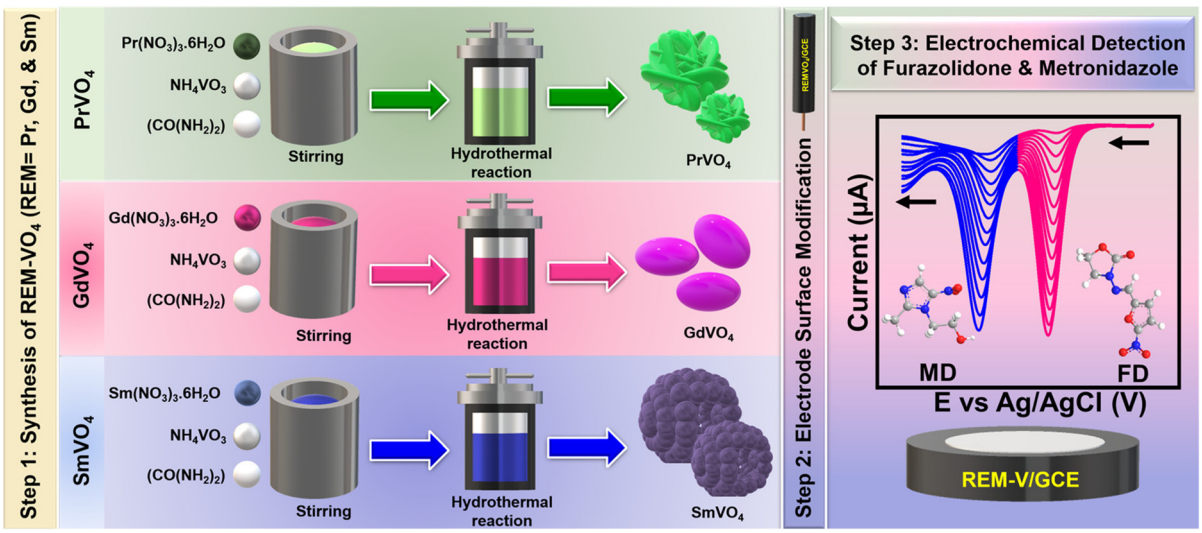

Scheme 2 A schematic representation of the synthesis of REM-VO_4.

phosphate buffer solution (PBS) between the potential range of −1.0 to +1.0 V. Simultaneously, 2 mg of the prepared $PrVO_4$ was dispersed in 1 mL of DI water and ultrasonicated for 15 min. Finally, 6 μL mg^{-1} from the above solution was used to modify the active surface of the GCE using the drop-casting method. The modified electrode was dried at 60 °C and denoted as PrV/GCE. In the same way, the other SmV/GCE and GdV/GCE electrodes were also prepared and modified.

2.4. Calculations

2.4.1. The Debye–Scherrer equation.

$$D = \frac{k\lambda}{\beta \cos\theta} \quad (1)$$

where, D = crystallite size, k = Scherrer's constant, λ = X-ray wavelength, θ = Bragg's angle, and β = full width at half-maximum.

2.4.2. The charge transfer rate (K_s).

$$K_s = \frac{RT}{n^2F^2R_{ct}C} \quad (2)$$

where, K_s = charge transfer coefficient, R = gas constant, n = number of electrons, F = Faraday constant, C = capacitance, and R_{ct} = charge transfer resistance.

2.4.3. Electrochemically active surface area (EASA). The electrochemically active surface area was calculated by the Randles–Sevcik equation.

$$I_p = 2.69 \times 10^5 n^{3/2} A D^{1/2} C v^{1/2} \quad (3)$$

where I_p = redox current, n = number of electrons involved (n = 1), A = electrochemically active surface area, D = diffusion coefficient of ferricyanide solution, C = concentration of the ferricyanide solution ($C = 5.0 \times 10^{-6}$ mol cm^{-3}) and v = potential of the scan rate (mV s^{-1}).

2.4.4. The charge transfer coefficient (α).

$$\Delta = \frac{n(1-\alpha)F}{2.3RT} \quad (4)$$

where, Δ = slope of Tafel plot, R = gas constant, n = number of electrons, F = Faraday constant, α = charge transfer coefficient, and T = temperature.

2.4.5. Calculation of the limit of detection (LOD). The LOD was measured by the following equation.

$$\mathrm{LOD} = \frac{3 \times \mathrm{SD}}{m} \quad (5)$$

where SD – standard deviation and the SD can be measured from the blank signal, m – slope value from the calibration plot.

2.4.6. The precision assay (relative standard deviation – RSD).

$$\mathrm{RSD} = \frac{100 \times \mathrm{SD}}{\text{mean of determination}} \quad (6)$$

2.4.7. The current retention.

$$\text{Current retention (\%)} = \frac{\text{final current} \times 100}{\text{inital current}} \quad (7)$$

3. Results and discussion

3.1. Structural and morphological analysis

3.1.1. Praseodymium vanadate ($PrVO_4$). The X-ray diffraction (XRD) analysis was performed to analyze the crystallographic parameters and purity of as-synthesized materials. The results obtained are refined using TOPAS software. Fig. 1A represents the Rietveld refinement plot of $PrVO_4$. The obtained XRD patterns are matched with JCPDS No: 00-017-0879 of the tetragonal crystal structure without any secondary phase. The refined crystallography parameters are as follows: space group = $I41/amd$, space group number = 141, $a = b$ = 7.3529 Å, c = 6.4600 Å, $\alpha = \beta = \gamma = 90°$, and the cell volume = 349.26 $Å^3$ which are nearly equal to the standard pattern (JCPDS No: 00-017-0879) of $PrVO_4$. Also, the obtained major planes such as (101), (200), (211), (112), (220), (301), (103), (321), (312), (400), (420), (332), (204), and (224) and their respective 2Theta values 18.2, 24.1, 30.5, 32.6, 34.4, 39.2, 43.7, 46.7, 48.2, 49.5, 55.8, 60.5, 62.7, and 68.2° are matched with the as-synthesized $PrVO_4$. The goodness of fit (GOF) is 1.08, nearly equal to 1. The average crystallite size (ACS) was calculated using the Debye–Scherrer equation (eqn (1)), and it shows 33.50 nm as the average crystallite size for $PrVO_4$. FT-IR spectroscopy was used to analyze the chemical bonding of $PrVO_4$. As marked in Fig. 1B, the peak obtained at 447.4 cm^{-1} and around 790.1 cm^{-1} corresponds to VO_4^{3-} and V–O–V vibrations. The bending vibration of the H_2O molecule occurred at 1630.9 cm^{-1}. Similarly, the peak at around 3000–3600 cm^{-1} is attributed to the O–H stretching vibration of the water molecule.[41,51] Furthermore, Fig. 1C shows the Raman analysis of the as-synthesized $PrVO_4$. The symmetrical stretching vibrations at 160.7, 302.3, and 421.4 cm^{-1} are ascribed to the external mode of $PrVO_4$. The asymmetric stretching vibration of VO_4^{3-} is found near 302.3 and 421.4 cm^{-1}. The predominant peak at 902.6 cm^{-1} is attributed to the tetrahedral VO_4^{3-} of $A1_g$ symmetric vibrations, and the vibration band at 837.6 cm^{-1} is ascribed to E_g asymmetric vibration.[41] Furthermore, XPS was performed to analyze the oxidation state of the as-synthesized materials. Fig. 1D depicts the overall spectrum, and Fig. S1A† shows the energy-dispersive X-ray spectrum (EDX) of $PrVO_4$ conforms to the presence of Pr, V, and O. The high-resolution spectrum of Pr 3d is shown in Fig. 1E. The Pr^{4+} peaks of $3d_{5/2}$ and $3d_{3/2}$ are observed at 927.1 eV and 947.6 eV respectively, whereas the binding energy values around 923.2 eV and 942.9 eV correspond to $3d_{5/2}$ and $3d_{3/2}$ of Pr^{3+}.[52] The deconvoluted spectrum of O 1s and V 2p is shown in Fig. 1F. The significant peak at 530.2 eV represents the M–O bond and the surface H_2O was observed at 532.9 eV. The nearby two substantial peaks at 517.6 eV and 525.0 eV binding energy correspond to V $2P_{3/2}$ and V $2P_{1/2}$ of V^{5+}.[53] TEM was used to analyze the morphological studies of $PrVO_4$. The image shows the flower-like structure of $PrVO_4$ and the average particle size is 890 nm (Fig. 1G). The crystallite size obtained is smaller than the particle size, which obeys Peter Dier's rule. According to Fig. 1H, the observed lattice fringe d = 0.341 nm is aligned with the (200) plane of $PrVO_4$. Fig. 1I displays the

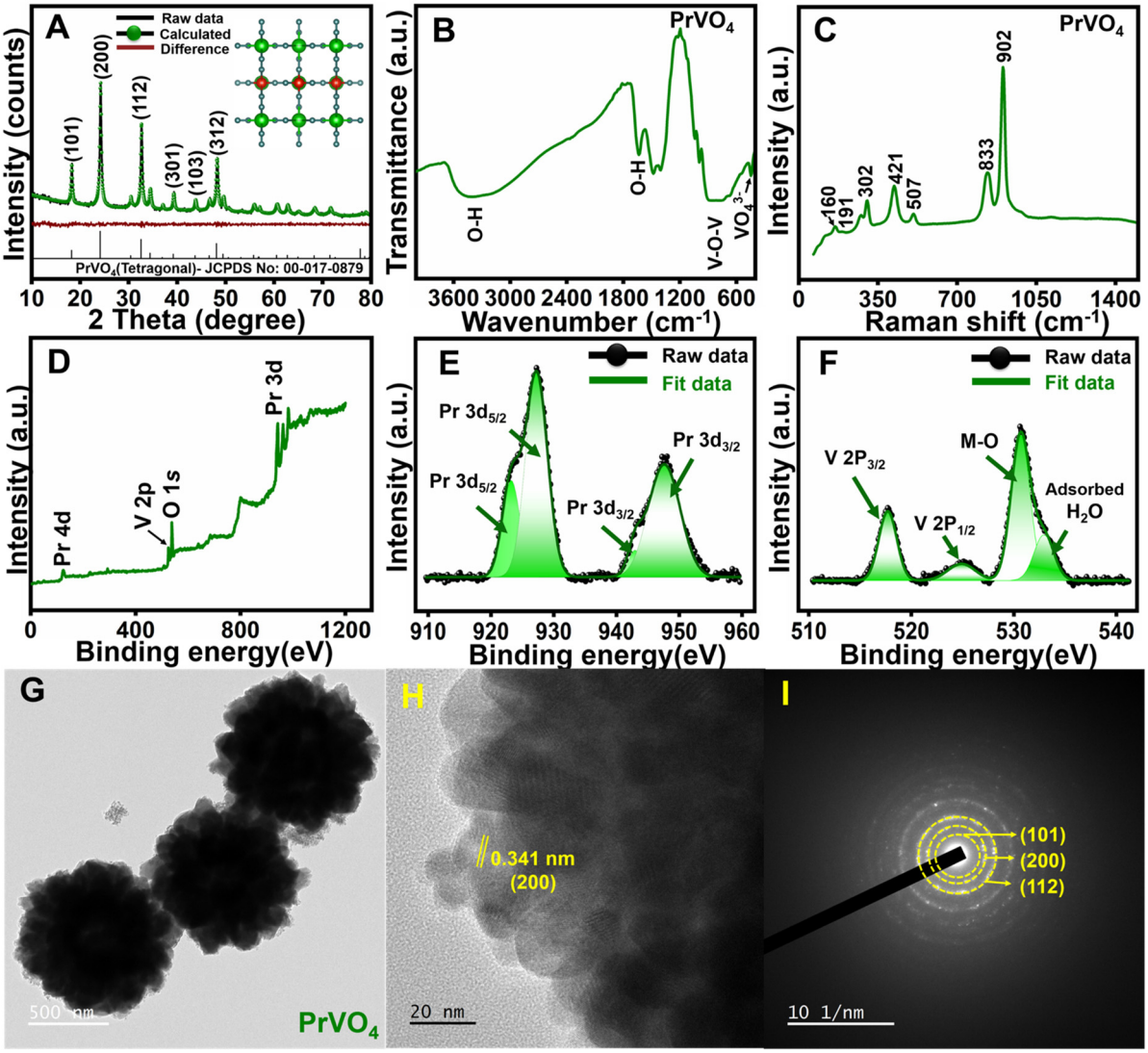

Fig. 1 (A) XRD, (B) FT-IR, (C) Raman, and XPS (D) overall survey spectrum of (E) Pr and (F) V and O. (G) TEM image, (H) lattice fringe, and (I) SAED pattern of $PrVO_4$.

SAED (selective area electron diffraction) pattern of $PrVO_4$, which conforms to the expansion of the crystalline structure along the (101), (200), and (112) planes of $PrVO_4$.

3.1.2. Gadolinium vanadate ($GdVO_4$). The Rietveld refinement plot of $GdVO_4$ is depicted in Fig. 2A. The acquired XRD pattern of $GdVO_4$ is compared to the standard JCPDS Pattern 00-017-0260, which corresponds to a tetragonal crystal system. The other crystallographic parameters are as follows: space group = *I*41/*amd*, space group number 141, $a = b = 7.2151$ Å, $c = 6.3436$ Å, $\alpha = \beta = \gamma = 90°$, and the cell volume = 330.25 Å^3 which are nearly equal to the standard pattern (JCPDS No: 01-086-0996) of $PrVO_4$. Also, the obtained major planes such as (101), (200), (211), (112), (220), (301), (103), (321), (312), (400), (420), and (332) and their respective 2Theta values 18.60, 24.65, 31.07, 33.23, 35.15, 40.06, 44.61, 47.60, 49.14, 50.55, 57.03, and 61.85° matched with those of the as-synthesized $GdVO_4$. The obtained GOF value is 1.01. The average crystallite size of $GdVO_4$ is 18.57 nm. The obtained FT-IR pattern of $GdVO_4$ is shown in Fig. 2B. The peaks observed at 455.1 cm^{-1} and near 809.1 cm^{-1} correspond to VO_4^{3-} and V–O–V vibration modes. The H_2O molecule exhibited a bending vibration with a frequency of 1635.4 cm^{-1}. The peak observed between 3000–3600 cm^{-1} is caused by the O–H stretching vibration of the water molecule. As shown in Fig. 2C, the symmetrical stretching vibrations at 153.7, 297.8, and 421.5 cm^{-1} result from the external mode of $GdVO_4$. VO_4^{3-} exhibits an asymmetric stretching vibration between 300.0 and 421.5 cm^{-1}. The main peak at 902.6 cm^{-1} is caused by the tetrahedral VO_4^{3-} ions vibrating in a symmetric manner ($A1_g$). The vibration band at 839.7 cm^{-1} is due to the asymmetric vibration of E_g. The overall XPS spectrum (Fig. 2D) and EDX spectrum (Fig. S1B†) of $GdVO_4$ validate the presence of Gd, V, and O. Fig. 2E displays the XPS spectrum of $GdVO_4$, where the two peaks at binding energies of 1186 eV and 1219.3 eV correspond

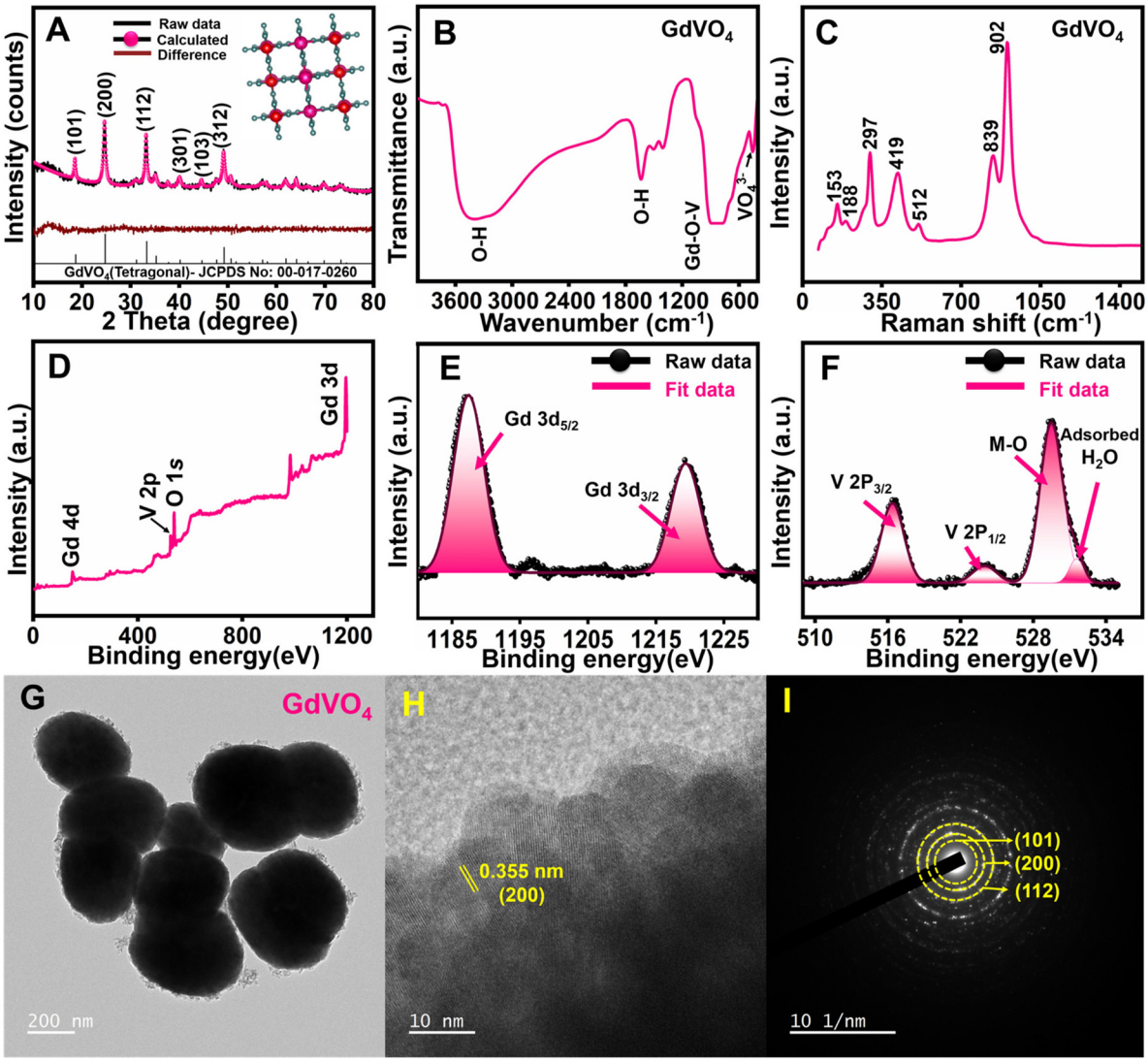

Fig. 2 (A) XRD, (B) FT-IR, (C) Raman, and XPS (D) overall survey spectrum, (E) Gd and (F) V and O. (G) TEM image, (H) lattice fringe, and (I) SAED pattern of $GdVO_4$.

to $3d_{5/2}$ and $3d_{3/2}$ of Gd.[54] The high-resolution spectrum of O 1s and V 2p is displayed in Fig. 2F. The 529.5 and 531.5 eV peaks are attributed to the M–O bond and adsorbed H_2O, respectively. The peaks with 517.6 eV and 525 eV binding energies correspond to V $2p_{3/2}$ and V$2p_{1/2}$ of V^{5+}.[53] In Fig. 2G the TEM results show an oval-like shape of $GdVO_4$, and the average particle size is 410 nm. Based on Fig. 2H, the measured lattice fringe with a distance of d = 0.355 nm aligns with the (200) plane of $GdVO_4$. Fig. 2I exhibits the SAED pattern of $GdVO_4$, which corresponds to the enlargement of the crystalline structure along the (101), (200), and (112) planes of $GdVO_4$.

3.1.3. Samarium vanadate ($SmVO_4$). Fig. 3A displays the Rietveld refinement plot of $SmVO_4$. Where the obtained XRD pattern of as-synthesized $SmVO_4$ is coordinated with standard JCPDS no. 00-017-0876. The refined crystallographic parameters are as follows: space group = *I*41/*amd*, space group number = 141, $a = b$ = 7.2575 Å, c = 6.3829 Å, $\alpha = \beta = \gamma = 90°$, and the cell volume = 336.20 Å^3 which are the closest to the standard pattern of $SmVO_4$. The distinct lattice planes such as (101), (200), (211), (112), (220), (301), (103), (321), (312), (400), (420), and (332) and their respective 2Theta values 18.49, 24.51, 30.88, 33.02, 34.93, 39.81, 44.33, 47.31, 48.83, 50.24, 56.67, and 61.44° correspond to those of the as-synthesized $SmVO_4$. The GOF value is 1.03. The average crystallite size of $SmVO_4$ is 22.72 nm. The O–H stretching vibration of the H_2O molecule was observed around a wavelength of 3000–3600 cm^{-1} (Fig. 3B). Similarly, the bending vibration of the H_2O molecule is found in the range of 1635.3 cm^{-1}. The 825.3 cm^{-1} and 455.1 cm^{-1} peaks correspond to the vibration modes of V–O–V and VO_4^{3-}, respectively. The primary peak in the Raman spectrum at 900.4 cm^{-1} shown in Fig. 3C is attributed to the symmetric vibration ($A1_g$) of VO_4^{3-} tetrahedra. Likewise, the vibration band observed at a wavenumber of

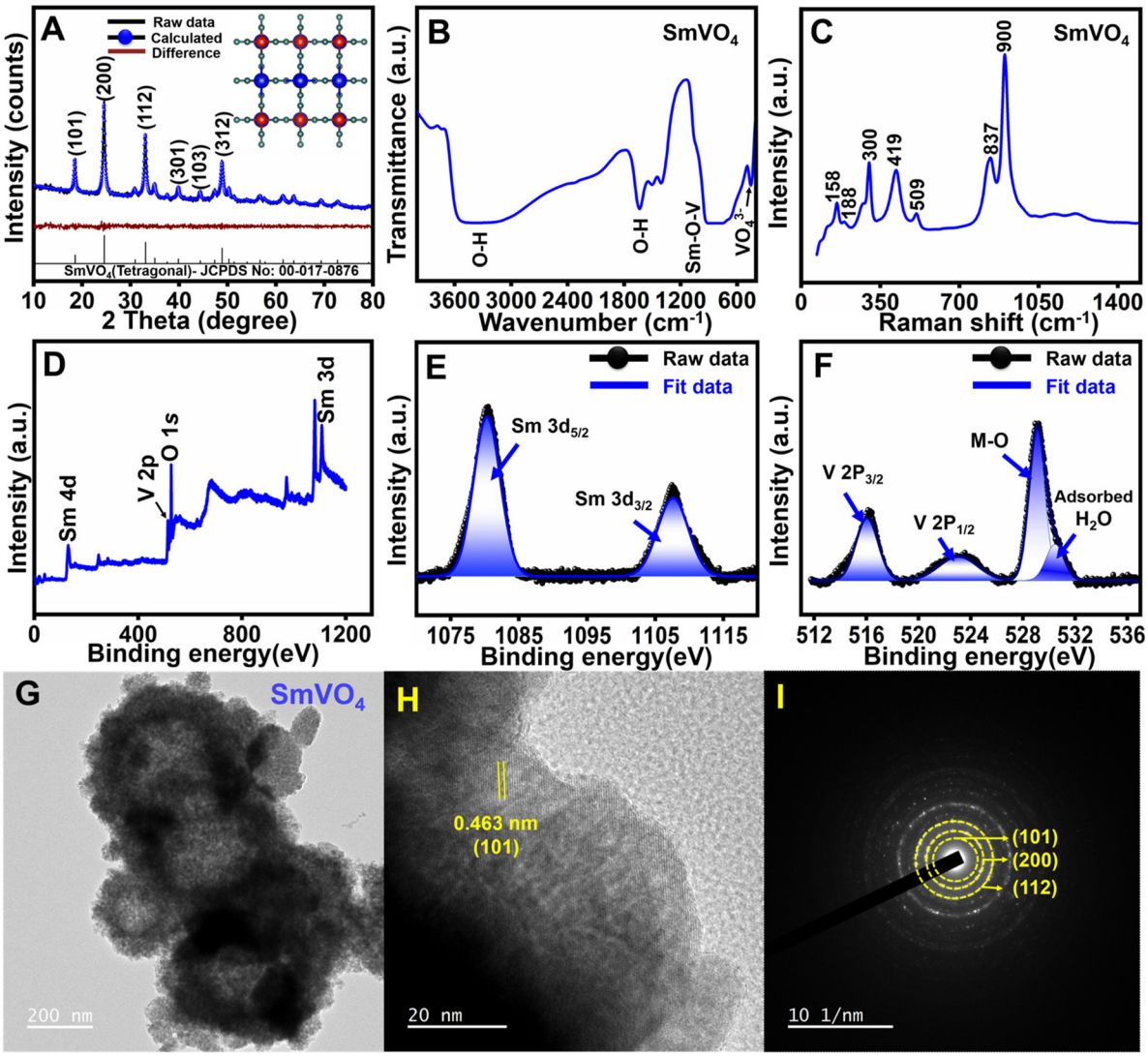

Fig. 3 (A) XRD, (B) FT-IR, (C) Raman, XPS of (D) overall survey spectrum, (E) Sm and (F) V and O. (G) TEM image, (H) lattice fringe, and (I) SAED pattern of $SmVO_4$.

837.6 cm^{-1} results from the E_g asymmetric vibration. The symmetrical stretching vibrations at 158.4, 300.1, and 419.2 cm^{-1} are attributed to the external mode of $SmVO_4$. The XPS and EDX spectra of $SmVO_4$, as shown in Fig. 3D and Fig. S1C,† confirm the presence of Sm, V, and O, respectively. The high-resolution XPS Sm 3d spectrum (Fig. 3E) shows two notable peaks at energy levels of 1080.1 eV and 1107.8 eV, attributed to the Sm $3d_{5/2}$ and Sm $3d_{3/2}$.[55] Fig. 3F shows the detailed spectrum of V 2p and O 1s. The peaks detected at 516.1 eV and 522.9 eV are ascribed to V $2p_{3/2}$ and V $2p_{1/2}$ of V^{5+}. The peak at a binding energy of 529.2 eV conforms to the M–O bond, and around 530.4 eV, the adsorbed H_2O was obtained.[53] In Fig. 3G, the TEM results reveal that $SmVO_4$ particles exhibit a hollow sphere morphology, with an average particle size of 430 nm. According to Fig. 3H, the lattice fringe measurement with a distance of d = 0.463 nm is aligned with the (101) plane of $SmVO_4$. Fig. 3I displays the SAED pattern of $SmVO_4$, which corresponds to the magnification of the crystal structure along the (101), (200), and (112) planes of $SmVO_4$.

3.1.4. Crystallographic parameters with rare earth metal site variation. As-synthesized zircon-type REM-based vanadates ($PrVO_4$, $GdVO_4$, and $SmVO_4$) exhibit a tetragonal crystal structure with space group *I*41/*amd* and space group number 141. The variation in the cationic sites of REMs leads to a significant change in the crystallographic parameters. Among the as-synthesized REMs, $PrVO_4$ has a large cell volume of 349.29 $Å^3$ due to the increased unit cell parameters $a = b$ = 7.3529 Å and c = 6.4600 Å. While the replacement of Pr with Sm in REM leads to a decrease in the cell volume (336.20 $Å^3$) and unit cell ($a = b$ = 7.2575 Å and c = 6.3829 Å). Furthermore, replacing Pr with Gd in the crystal structure leads to the lowering of the cell volume (330.25 $Å^3$) and unit cell parameters ($a = b$ = 7.2151 Å and c = 6.3436 Å). This trend may be attributed to the decreasing ionic radii from Pr to Gd. According to the Braggs law, the

large unit cell observed in $PrVO_4$ shifts the observed XRD plane to the lower angle side. Instead, the lower unit cell of $GdVO_4$ shifts the observed XRD pattern to the side with a higher angle. As a result, the (200) planes of $PrVO_4$, $SmVO_4$, and $GdVO_4$ were observed at 2Theta values of 24.10, 24.51, and 24.65, respectively. Similarly, the average crystal size calculated using the Debye–Scherrer Equation replicates the same trend. The obtained average crystallite size in the increasing order is: $GdVO_4$ (18.57 nm) < $SmVO_4$ (22.72 nm) < $PrVO_4$ (33.50 nm). Table 1 shows Rietveld refinement XRD parameters of REM-VO_4 (REM = Pr, Gd, and Sm). Furthermore, Peter Dier's rule says that the crystallite size is less than the grain size, and the grain size is lesser than the particle size. According to this, the average particle size of the as-synthesized $GdVO_4$ (410 nm) < $SmVO_4$ (430 nm) < $PrVO_4$ (890 nm) is higher than its respective crystallite size. Similarly, Table S1† represents the Raman vibration modes and Table S2† portrays the respective binding energy values of as-synthesized REM-VO_4 (REM = Pr, Gd, and Sm). Though the $SmVO_4$ and $GdVO_4$ have nearly similar crystallographic parameters, the hollow nature and nanoparticle size of $SmVO_4$ make it a superior candidate for the electrochemical detection of FD and MD.

3.2. Electrochemical impedance spectroscopy

Electrochemical impedance spectroscopy (EIS) is a commonly employed method for studying the characteristics of the interface between an electrolyte and an electrode. The Randels's circuit consisting of solution resistance (R_s), charge transfer resistance (R_{ct}), Warburg impedance (Z_w), and double-layer capacitance (C_{dl}) is used to analyze the obtained impedance. The combination of $K_3[Fe(CN)_6]$ and $K_4[Fe(CN)_6]$ was used as a redox probe to study the charge transfer resistance (R_{ct}) and the Warburg impedance (Z_w) of the as-synthesized REM-VO_4. The R_{ct} refers to the semicircle obtained at a higher- frequency of the plot and the Z_w represents the straight line of the plot at lower frequencies. The smaller the semicircle and the closer the straight line towards the *y*-axis, the higher the material's conductivity. Since the R_s depends upon the concentration of the redox probe and is constant for all the electrodes, there is no appreciable difference in the R_s value of all the modified electrodes.[56,57] Fig. S2A† displays the Nyquist plot of different modified electrodes. Among all the electrodes, the bare-GCE shows an enormous semicircle (R_s = 88.0 Ω and R_{ct} = 278.6 Ω) with higher resistance due to the lack of active surface area and sluggish electron transportation. A decreased R_{ct} value (R_s = 90.1 Ω and R_{ct} = 205.1 Ω) was obtained for the PrV/GCE when compared to the bare-GCE due to the infusion of nanomaterials, which helps to increase the active surface of the electrode. When compared to bare-GCE and PrV/GCE, GdV/GCE shows a low R_{ct} value of 130.0 Ω (R_s = 88.2 Ω) due to smaller particle size, which could afford more electrochemical active sites for electron transport. Due to the hollow nature of the $SmVO_4$, the ions can effectively diffuse into the interface, and an electrochemical reaction occurs. As a result, an effective electron transfer occurred, and the lowest R_{ct} = 56.8 Ω and R_s = 87.7 Ω values were obtained compared to all the electrodes. Furthermore, the charge transfer rate (K_s) was calculated using eqn (2). As evident from the EIS results, the highest K_s value of 7.86×10^{-8} was exhibited by the SmV/GCE, which indicates the increased rate of electron transportation due to the low resistance. Table S3† compares the modified electrodes' R_s, R_{ct}, ESR (equivalent series resistance), and K_s values.

3.3. Electrochemically active surface area

Furthermore, the electrochemical activities of the modified electrodes were evaluated by cyclic voltammetry (CV) in $K_3[Fe(CN)_6]$ and $K_4[Fe(CN)_6]$ redox probes (Fig. S2B†). All the electrodes exhibit one significant oxidation and reduction peaks, respectively. The obtained redox peaks correspond to the following conversions (8) and (9).[58]

$$Fe(CN)_6^{4-} \xrightarrow{\text{oxidation}} Fe(CN)_6^{3-} + e^- \quad (8)$$

$$Fe(CN)_6^{3-} + e^- \xrightarrow{\text{reduction}} Fe(CN)_6^{4-} \quad (9)$$

The bare GCE shows the lowest redox peak current (I_{pa} = 70.62 μA and I_{pc} = −66.98 μA) and poor peak-to-peak separation (ΔE = 0.30 V) among all the modified electrodes due to its diminished electron transfer rate. Instead, the PrV/GCE and GdV/GCE showed improved redox peak currents, and the respective redox peaks significantly shifted to the negative side. The respective ΔE values of PrV/GCE and GdV/GCE are 0.17 V and 0.14 V. Similarly, their respective redox peak current values are I_{pa} = 92.18 μA and I_{pc} = −90.75 μA (PrV/GCE) and I_{pa} = 101.5 μA and I_{pc} = −98.39 (GdV/GCE). As proof of EIS results, the electrode modified with $SmVO_4$ (SmV/GCE) shows the maximum redox peak current of I_{pa} = 110.00 μA and I_{pc} = −103.70 μA in a potential range of E_{pa} = 0.28 V and E_{pc} = 0.16 V, respectively. In addition, the SmV/GCE exhibited a low peak-to-separation value of ΔE = 0.12 V. All the modified electrodes show that the I_{Pa}/I_{Pc} ratio is approximately one, revealing that

Table 1 The Rietveld refinement XRD parameters of REM-VO_4 (REM = Pr, Gd and Sm)

REM-VO_4	$a = b$ (Å)	c (Å)	$\alpha = \beta = \gamma$	Cell volume (Å^3)	R_{exp}	R_{wp}	R_p	GOF	ACS (nm)
$PrVO_4$	7.3529	6.4600	90°	349.26	4.26	4.60	3.51	1.08	33.50
$GdVO_4$	7.2151	6.3436	90°	330.25	2.92	2.95	2.33	1.01	18.57
$SmVO_4$	7.2575	6.3829	90°	336.20	3.29	3.40	2.70	1.03	22.72

R_{exp} – expected residual factor, R_{wp} – weighted profile residual factor, R_p – profile residual factor, GOF – goodness of fit; ACS – average crystallite size.

the number of electrons involved in the oxidation and reduction process is the same. Furthermore, to evaluate the electrochemically active surface area (EASA), the CV was performed at different scan rates for all the modified electrodes. As observed in Fig. S2C & S3(A, C, E)† on increasing the scan rate from 0.02 V s^{-1} to 0.2 V s^{-1} the redox peak current also increases gradually and the corresponding linear plot of the square root of scan rate *vs.* redox peak current is given in Fig. S2D and S3(B, D, F).† This square root of scan rate *vs.* redox peak current confirms that all the modified electrodes follow the diffusion control process. The respective linear regression equations are as follows:

Bare-GCE

$$I_{pa}\ (\mu A) = 266.91\ (V\ s^{-1})^{1/2} + 11.734; \quad R^2 = 0.9995 \quad (10)$$

$$I_{pc}\ (\mu A) = -174.21\ (V\ s^{-1})^{1/2} - 26.418; \quad R^2 = 0.9905 \quad (11)$$

PrV/GCE

$$I_{pa}\ (\mu A) = 332.81\ (V\ s^{-1})^{1/2} + 20.978; \quad R^2 = 0.9983 \quad (12)$$

$$I_{pc}\ (\mu A) = -251.06\ (V\ s^{-1})^{1/2} - 31.356; \quad R^2 = 0.9925 \quad (13)$$

GdV/GCE

$$I_{pa}\ (\mu A) = 385.36\ (V\ s^{-1})^{1/2} + 20.165; \quad R^2 = 0.9982 \quad (14)$$

$$I_{pc}\ (\mu A) = -292.13\ (V\ s^{-1})^{1/2} - 30.651; \quad R^2 = 0.9945 \quad (15)$$

SmV/GCE

$$I_{pa}\ (\mu A) = 390.85\ (V\ s^{-1})^{1/2} + 21.90; \quad R^2 = 0.9973 \quad (16)$$

$$I_{pc}\ (\mu A) = -312.97\ (V\ s^{-1})^{1/2} - 29.32; \quad R^2 = 0.9953 \quad (17)$$

The R^2 value of the modified electrodes is nearly equal to one, and their respective active surface area was calculated using the Randles–Sevick equation (eqn (3)).[59–61] The SmV/GCE shows the highest active surface area A = 0.11 cm^2 due to more active sites. In contrast, other modified electrodes show 0.10 cm^2 (GdV/GCE), 0.09 cm^2 (PrV/GCE), and 0.07 cm^2 (bare GCE). Table 2 summarizes the I_{pa}, I_{pc}, I_{pa}/I_{pc}, E_{pa}, E_{pc}, ΔE, and A of modified electrodes.

Table 2 The CV parameters of REM-VO_4 (REM = Pr, Gd, and Sm) in the redox medium

Modified electrodes	I_{pa} (μA)	E_{pa} (V)	I_{pc} (μA)	E_{pc} (V)	ΔE	I_{pa}/I_{pc}	A (cm^2)
Bare-GCE	70.62	0.38	−66.98	0.08	0.30	1.05	0.07
PrV/GCE	92.18	0.31	−90.75	0.14	0.17	1.01	0.09
GdV/GCE	101.50	0.29	−98.39	0.15	0.14	1.03	0.10
SmV/GCE	110.00	0.28	−103.70	0.16	0.12	1.06	0.11

3.4. Electrochemical behaviors of the as-modified electrodes towards furazolidone and metronidazole

Fig. 4A shows the DPV results of modified electrodes (REM-V/GCE; REM-Pr, Gd, and Sm) towards FD in 0.1 M PBS. All the electrodes show one major reduction peak between the potential range of −0.38 and −0.41 V, corresponding to the FD nitro group reduction. The bare-GCE exhibits the lowest cathodic current ($I_{pc(FD)}$ = −9.07 μA) due to poor electron transportation and lack of active sites. The GCE modified with flower-like $PrVO_4$ nanoparticles (PrV/GCE) enhances the catalytic behavior

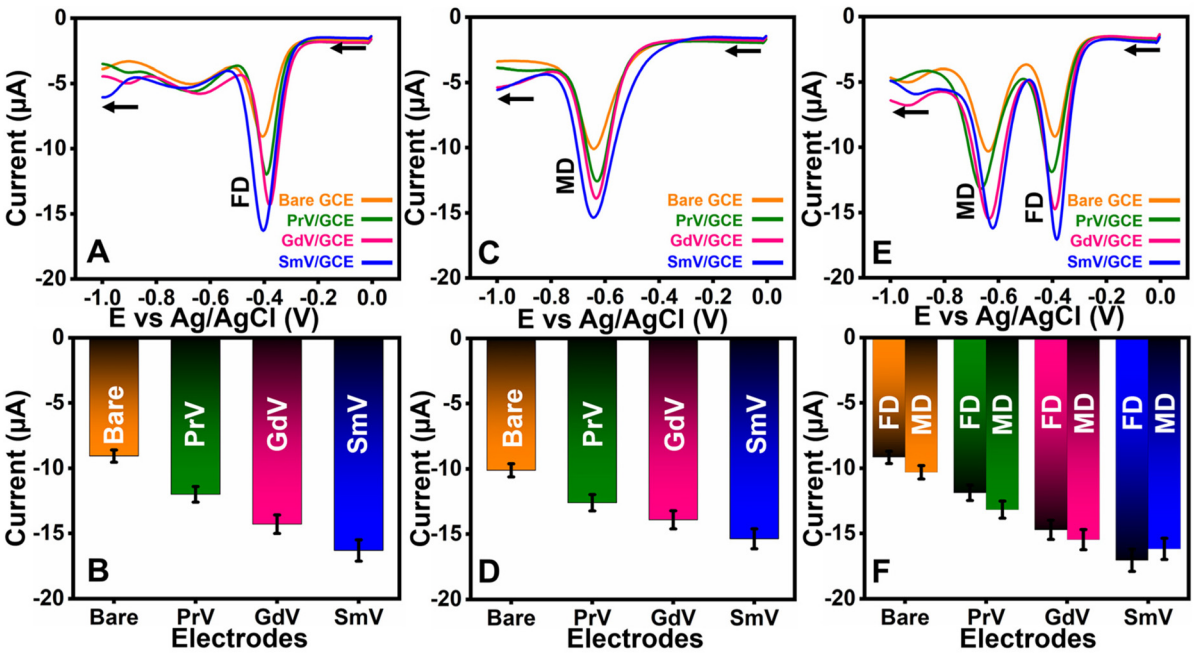

Fig. 4 DPV profiles of the modified electrode in the presence of (A) FD, (C) MD, (E) FD and MD, and (B, D and F) respective bar diagrams.

of the GCE by increasing the reactive sites on the surface of the GCE, which results in increased cathodic current ($I_{pc(FD)}$ = −11.98 μA) than the bare-GCE. On comparing the GdV/GCE with PrV/GCE, the $GdVO_4$ has a smaller particle size than the as-synthesized $PrVO_4$ (from the TEM results). This leads to an increase in the surface area of GdV/GCE and increases the adsorption of more FD molecules. As a result, GdV/GCE shows a higher reduction current of $I_{pc(FD)}$ = −14.30 μA than bare-GCE and PrV/GCE. Though $SmVO_4$ has a relatively larger particle size than $GdVO_4$ but not larger than $PrVO_4$, the distinct nano-hollow structure of the as-synthesized $SmVO_4$ provides high permeability of FD into the SmV/GCE active sites and helps to shorten the electron transfer path.[62] This makes the SmV/GCE show increased sensing behavior than the other modified and bare GCE towards FD with the highest cathodic current of $I_{pc(FD)}$ = −16.28 μA. Fig. 4B presents a bar diagram of modified electrodes *vs.* the current of FD.

Fig. 4C depicts the DPV results of modified electrodes towards MD in 0.1 M PBS. A significant cathodic current was observed in the potential range of 0.63–0.64 V of modified electrodes due to the reduction of the nitro group of the MD. Similar to the results of FD detection, the bare-GCE exhibited the poorest response amid ($I_{pc(MD)}$ = −10.10 μA) all electrodes. Followed by the PrV/GCE ($I_{pc(MD)}$ = −12.58 μA) and GdV/GCE ($I_{pc(MD)}$ = −13.88 μA), which stand next to each other in the order of increasing cathodic current. Likewise, the SmV/GCE shows the highest current response ($I_{pc(MD)}$ = −15.35 μA) towards MD. Fig. 4D shows the bar diagram of modified electrodes *vs.* the current of MD.

Fig. 4E portrays the simultaneous DPV results of modified electrodes towards FD and MD in 0.1 M PBS. For the simultaneous detection, both the FD and MD are added at an equal concentration in PBS. In the same way, the two intended cathodic peaks are attributed to the FD and MD caused by nitro group reduction. The reduction peak between 0.38–0.40 V and 0.62–0.66 V corresponds to FD and MD, respectively. The participation of two analytes (FD and MD) simultaneously brings minor differences in their potential range compared to their potential. Also, only a negligible current difference is observed compared to their current response. Overall, the SmV/GCE has the highest current response ($I_{pc(FD)}$ = −17.07 μA and $I_{pc(MD)}$ = −16.19 μA) compared to all other electrodes. Moreover, the obtained results from the simultaneous detection of FD and MD (Fig. 4E) validate the results shown in Fig. 4A and C. Fig. 4F displays the bar diagram of modified electrodes *vs.* the current of FD and MD. Finally, the decreasing order of anodic current for the detection of FD, MD, and (FD and MD) is as follows: SmV/GCE > GdV/GCE > PrV/GCE > bare-GCE. So, the SmV/GCE was chosen as the optimum for further optimization. Table S4† summarizes the modified electrodes' potential and current response towards the FD and MD. Furthermore, to check the ability of the SmV/GCE by keeping one analyte at a fixed concentration, another concentration of the analyte was increased. Fig. 5A shows the simultaneous DPV results of the SmV/GCE, where the MD concentration was fixed, and the concentration of FD was increased from 20 μM to 100 μM. Similarly, in Fig. 5B the concentration of the FD was fixed and the MD concentration was increased from 20 μM to 100 μM. Both the results confirm that the presence of one analyte (FD or MD) will not affect the current response of another analyte concentration. The respective linear plot shows the R^2 values to be nearly equal to 1.

The effective surface area and mass transport limitations are the critical parameters that influence the sensing capacity of the electrodes. So, the effect of catalytic loading amount on the GCE surface was evaluated by varying the loading amount of $SmVO_4$. Fig. 6A shows the DPV results of SmV/GCE by varying the amount of $SmVO_4$ from 2–8 μL mg^{-1} in 0.1 M PBS with the presence of FD and MD. On increasing the loading amount of $SmVO_4$ from 2 μL mg^{-1} to 6 μL mg^{-1}, the cathodic

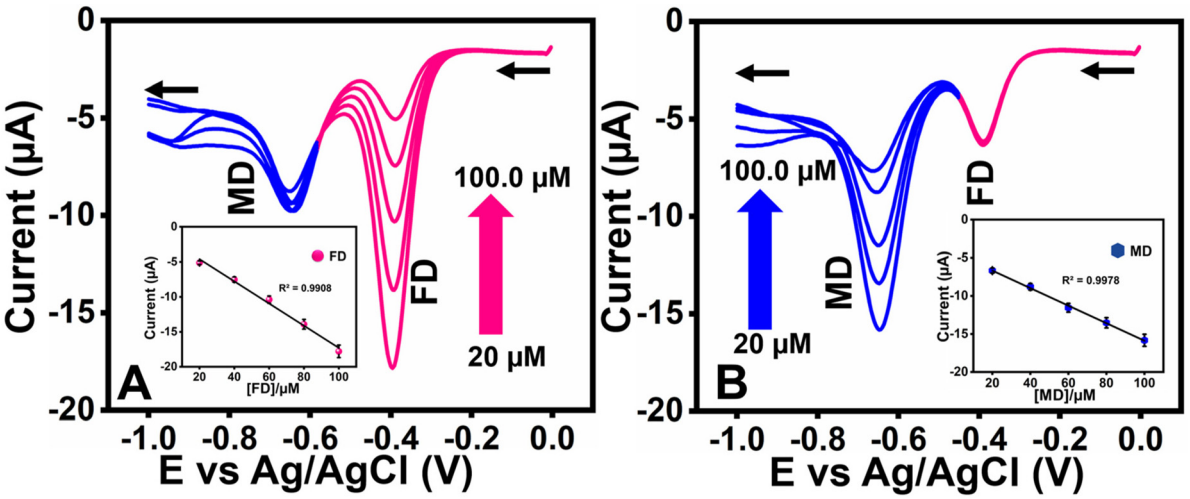

Fig. 5 DPV response of SmV/GCE with (A) consecutive additions of FD (20–100 μM) at a fixed concentration of MD and (B) consecutive additions of MD (20–100 μM) at a fixed concentration of FD (Inset: linear plot of concentration *vs.* peak current).

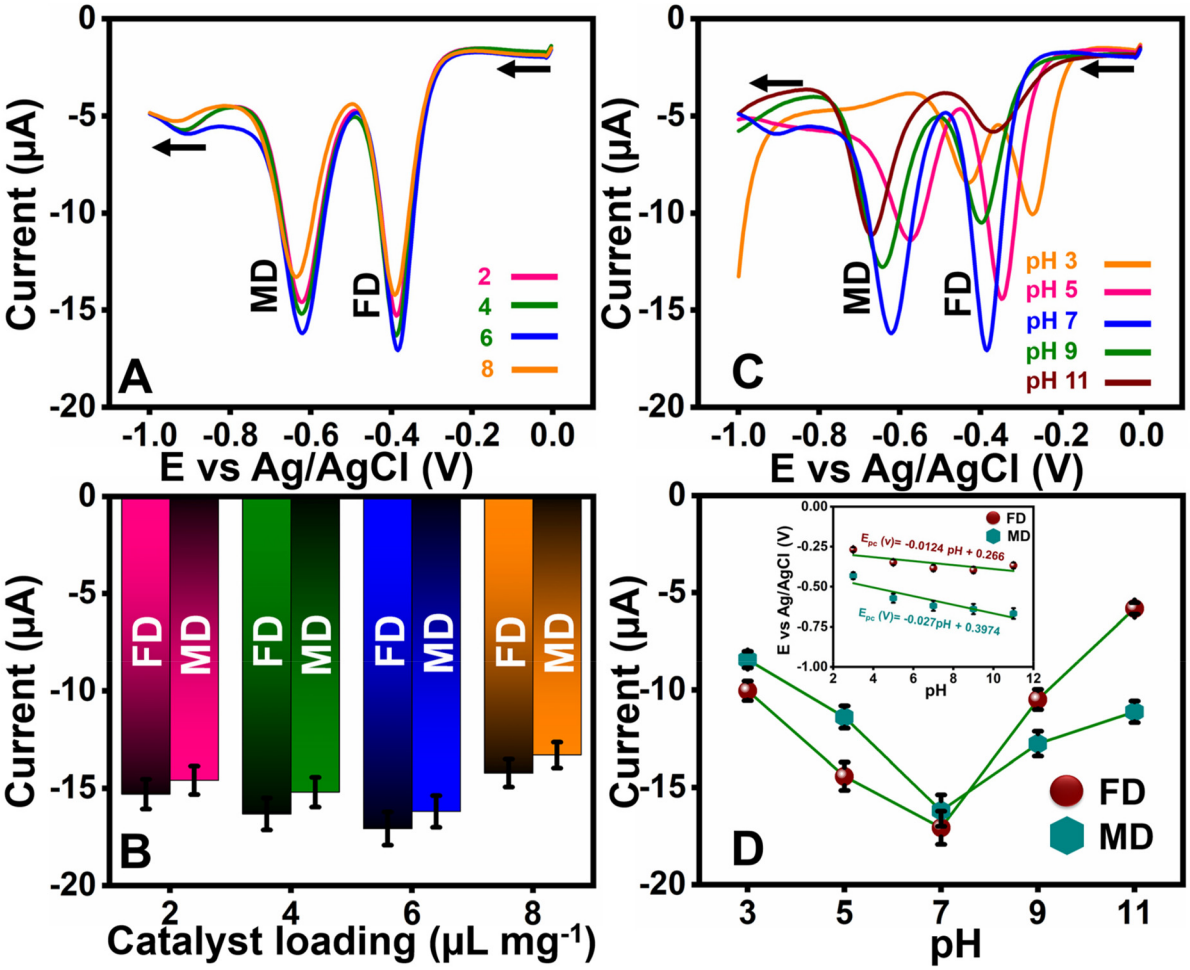

Fig. 6 DPV response of SmV/GCE (A) at different loading amounts (2–8 μL mg^{-1}), (B) bar diagram of catalyst loading *vs.* current, (C) at different pH values (3–11 pH), and (D) corresponding plot of pH *vs.* current (inset: pH *vs.* potential).

current response increased simultaneously. This is due to the increase in the surface area of the GCE due to the deposition of $SmVO_4$. The increase in the surface area can help increase the number of capture probes, which leads to the capture of more FD and MD into the active sites and increases the sensing capacity of the electrode. However, further increasing the loading amount of $SmVO_4$ causes a considerable drop in the cathodic current. This is attributed to the limitation of mass transport.[63] This means that as the loading amount of $SmVO_4$ exceeds 6 μL mg^{-1}, the coating on the GCE surface becomes thicker, which hinders the infiltration of the FD and MD into the active site of the GCE due to the accumulation of more $SmVO_4$ on the surface. Additionally, due to the electrode surface saturation, the reduction peak of 8 μL mg^{-1} is slightly shifted from the other peaks. The two parameters, such as active surface area and mass transportation, are balanced in a 6 μL mg^{-1} loading amount; as a result, the highest cathodic current response was observed. The decreasing order of anodic current for the effect of catalytic loading amount is as follows: 6 μL mg^{-1} ($I_{pc(FD)}$ = −17.07 μA and $I_{pc(MD)}$ = −16.19 μA) > 4 μL mg^{-1} ($I_{pc(FD)}$ = −16.32 μA and $I_{pc(MD)}$ = −15.20 μA) > 2 μL mg^{-1} ($I_{pc(FD)}$ = −15.30 μA and $I_{pc(MD)}$ = −14.59 μA) > 8 μL mg^{-1} ($I_{pc(FD)}$ = −14.22 μA and $I_{pc(MD)}$ = −13.30 μA). So, 6 μL mg^{-1} was chosen as the optimum loading amount for further optimization. Fig. 6B presents a bar diagram of catalyst loading *vs.* the current of FD and MD.

The cathodic/anodic current response can vary based on the supporting electrolyte medium's pH because of protons' involvement in an overall electrode reaction.[64] Fig. 6C shows the DPV results of SmV/GCE by changing the pH from 3–9 pH in 0.1 M PBS in the presence of FD and MD. On increasing the pH 3–7, the cathodic current response of FD and MD is increased along with the shift towards the negative potential side. The shift in the potential range is attributed to the involvement of the proton during the reduction of FD and MD. The current response significantly decreased by increasing pH to the basic medium (pH 9 and 11) due to the hydrolysis. Where both the FD and MD show the highest current response ($I_{pc(FD)}$ = −17.07 μA and $I_{pc(MD)}$ = −16.19 μA) in the neutral (pH 7) pH medium. The following equations could

explain the diminished current response in the acidic and basic medium.[65]

$$RNO_2 + e^- \rightleftarrows RNO_2^{\bullet -} \quad (18)$$

$$RNO_2^{\bullet -} + 3e^- + 4H^+ \rightleftarrows RNHOH + H_2O \quad (19)$$

The increased concentration of protons under acidic medium (pH 3 and 5) conditions leads to a higher degree of protonation of the anionic radical of the nitro group which is unable to take part in the reduction reaction (eqn (18)). Furthermore, in the alkaline medium (pH 9 and 11) there is a drop in the proton concentration, thereby a decreased anodic current was observed (eqn (19)). So, pH 7 was chosen as the optimum one for further optimization. Fig. 6D portrays the plot of pH *vs.* the current of FD and MD. Additionally, the pH *vs.* potential plot shows the linear regression equation for FD, $E = -0.0124$ and pH = 0.266 and for MD $E = -0.027$ and pH = 0.3974, where the slope values −0.0124 V per pH and $E = -0.027$ V per pH differ from the theoretical value of the Nernst equation. This indicates that the number of protons and electrons that participated in the cathodic reaction is not the same, as reported by Nguyen Tuan Anh *et al.* and Dao Thi Nguyet Nga *et al.*[66,67]

3.5. Electrochemical reduction mechanism of FD

As illustrated in Scheme 3A, the reduction of FD at the electrode surface proceeds in two distinct steps.

Step 1: Reduction of the nitro group to the nitroso intermediate

The first step in the reduction process involves the electrochemical reduction of the nitro group ($-NO_2$) present in the FD molecule. The nitro group ($-NO_2$) undergoes a two-electron reduction to form the nitroso species, which is a highly reactive intermediate. This step is crucial because it facilitates the transition from the nitro form to a more easily reduced species, the nitroso group.

$$R\text{–}NO_2 + 2e^- + 2H^+ \rightarrow R\text{–}N{=}O + H_2O$$

Step 2: Conversion of the nitroso intermediate to hydroxylamine

In the second step, the nitroso intermediate (R–N=O) undergoes a rapid reduction, converting into hydroxylamine (R–NHOH). This process involves the addition of hydrogen ions and electrons to the nitroso intermediate, resulting in the formation of hydroxylamine, a more stable and reduced species. This step is typically fast and completes the reduction of the nitro group into its final reduced form.

$$R\text{–}N{=}O + 2e^- + 2H^+ \rightarrow R\text{–}NHOH$$

The formation of hydroxylamine is important because it marks the completion of the electrochemical reduction, and this transition is primarily responsible for the observed reduction peak in the voltammetric behaviour of FD.

3.6. Electrochemical reduction mechanism of MD

Similarly, the electrochemical reduction of MD also follows a two-step mechanism, as outlined in Scheme 3B

Step 1: Formation of the nitro radical anion ($-NO_2^{\bullet -}$)

The first step in the reduction of MD involves the electron reduction of the nitro group ($-NO_2$) to form a nitro radical anion ($-NO_2^{\bullet -}$). This radical species is highly reactive and unstable but can be further reduced in the subsequent step. The reduction of the nitro group to its radical anion is a key step in the electron transfer process, enabling further transformation of the nitro group into the reduced product.

$$R\text{–}NO_2 + e^- + 2H^+ \rightarrow R\text{–}NO_2^{\bullet} + e^-$$

Step 2: Conversion of the nitro radical anion to hydroxylamine

The nitro radical anion ($-NO_2^{\bullet -}$) formed in the first step is quickly converted into hydroxylamine (R–NHOH) *via* the addition of electrons and protons. This rapid transformation marks the completion of the reduction process and contributes to the reduction peak observed during the electrochemical analysis of MD. The hydroxylamine (R–NHOH) is the stable

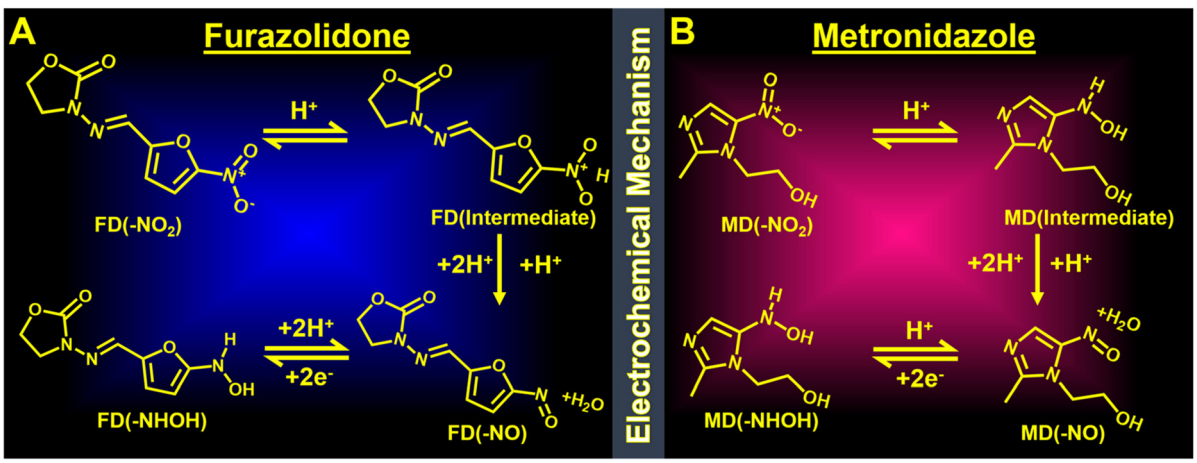

Scheme 3 Electrochemical mechanism of (A) FD and (B) MD.

reduced form, and its formation results in a measurable current in electrochemical measurements.

$$R\text{–}NO_2^{\bullet} + 2e^- + 2H^+ \rightarrow R\text{–}NHOH$$

Both FD and MD undergo similar reduction processes, with the nitro group first reduced to an intermediate (nitroso for FD and nitro radical for MD), followed by the formation of the final hydroxylamine product. These mechanisms underline the electron transfer processes at play during the electrochemical reduction and explain the observed reduction peaks in cyclic voltammetry or other electrochemical methods.

To study the electron transfer kinetics of SmV/GCE, the scan rate was varied from 0.02 V s^{-1} to 0.22 V s^{-1} in 0.1 M PBS with FD and MD. The scan results in Fig. S4A† show that the cathodic peak current of FD and MD increased linearly with the increase in the scan rate. The perfect reduction peak was obtained at lower scan rates due to the sufficient time for the interaction between the electrode and the electrolyte. On increasing the scan rate, the time for electrode–electrolyte interaction is reduced. As a result, the cathodic peaks shift toward the negative potential side. Fig. S4B† portrays the linear plot of scan rate *vs.* current where the R^2 values are nearly equal to one, confirming that the SmV/GCE follows the surface/adsorption control process.

FD:

$$I_{pc}\ (\mu A) = -21.224\ (V\ s–) - 5.8407; \quad R^2 = 0.9992 \qquad (20)$$

MD:

$$I_{pc}\ (\mu A) = -42.448\ (V\ s^{-1}) - 9.4663; \quad R^2 = 0.9912 \qquad (21)$$

Furthermore, Fig. S4C and D† present the relationship between the scan rate *vs.* cathodic peak potential, which confirms the linear shift in the peak potential on increasing the scan rate and the corresponding R^2 values 0.9980 (FD) and 0.9969 (MD) are approximately equal to one. Fig. S4E and F† show the linear plot of potential *vs.* log of current, which is used to determine the charge transfer coefficient (α). The α value was calculated using eqn (4), and it shows α = 0.75 for FD and α = 0.73 for MD.[68,69]

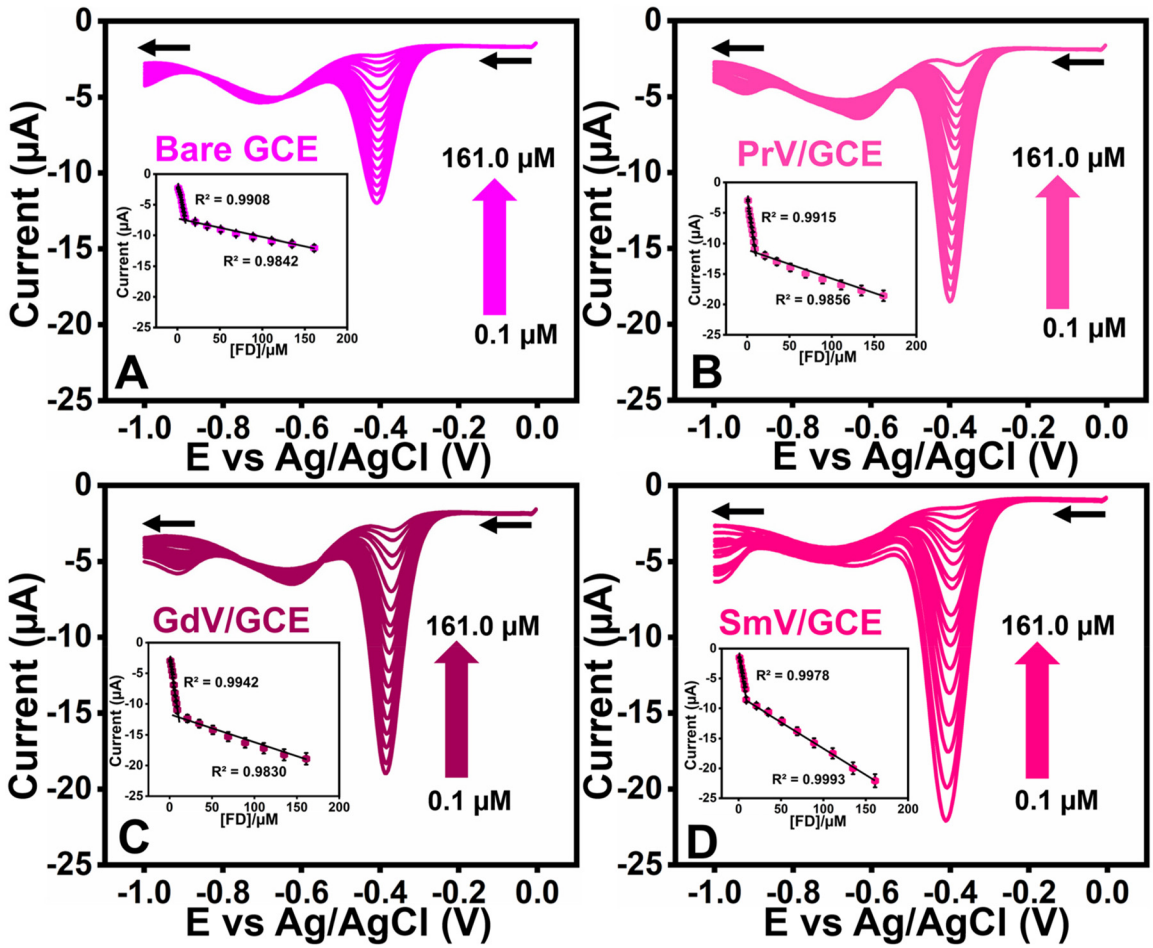

Fig. 7 DPV response of (A) bare GCE, (B) PrV/GCE, (C) GdV/GCE, and (D) SmV/GCE at different concentrations of FD (inset: respective linear plots of concentration *vs.* current).

3.7. Distinct and simultaneous determination of furazolidone and metronidazole

The DPV method was employed for the detection since it offers low background current, good selectivity, and sensitivity with rapid measurement. The applied DPV parameters are: applied potential – 0 to −1.0 V; sensitivity – 1×10^{-005}; pulse period – 0.5 s and amplitude – 0.05 V. Initially, to know the detection limit of the modified and un-modified electrodes towards FD and MD, the DPV was performed individually for both FD and MD. Fig. 7(A–D) and 8(A–D) show the DPV result of FD and MD in 0.1 M PBS. The FD and MD concentration range was kept constant for all the electrodes (0.1 μM–161.0 μM). On increasing the concentration of the FD and MD the cathodic peak current also increased linearly. The respective linear plots of concentration *vs.* current show two linear lines corresponding to lower and higher concentrations. However, the R^2 values for the electrodes are nearly equal to 1, representing a good linear relationship between the concentration and the current. The limit of detection (LOD) was calculated by eqn (5).[70,71] The bare GCE shows a reduced cathodic current towards the FD and MD due to the poor catalytic behavior of the bare GCE. Since the bare GCE shows the highest LOD (FD = 0.5245 μM and MD = 0.9302 μM) compared to the modified electrodes, it highlights the necessity of electrode modification to lower the LOD. Modifying the GCE with $PrVO_4$ and $GdVO_4$ nanoparticles could enlarge the surface area for the adsorption of FD and MD, which would help to reduce nitro to hydroxylamine conversion effectively. As a result, the increased cathodic and lower LOD was observed for PrV/GCE (FD = 0.0125 μM and MD = 0.0361 μM) and GdV/GCE (FD = 0.0089 μM and MD = 0.0160 μM).[72] The SmV/GCE has an additional advantage of a hollow nature and nanoparticle size compared to PrV/GCE and GdV/GCE. The hollow $SmVO_4$ nature provides sufficient diffusion channels and could enhance mass transportation of the FD and MD. As discussed, a hollow structure provides good contact with the electrode and electrolyte, providing a large specific surface area for FD and MD interactions. Moreover, the hollow structure with an adsorption enrichment effect, makes the cathodic response of SmV/GCE stand with the highest current response

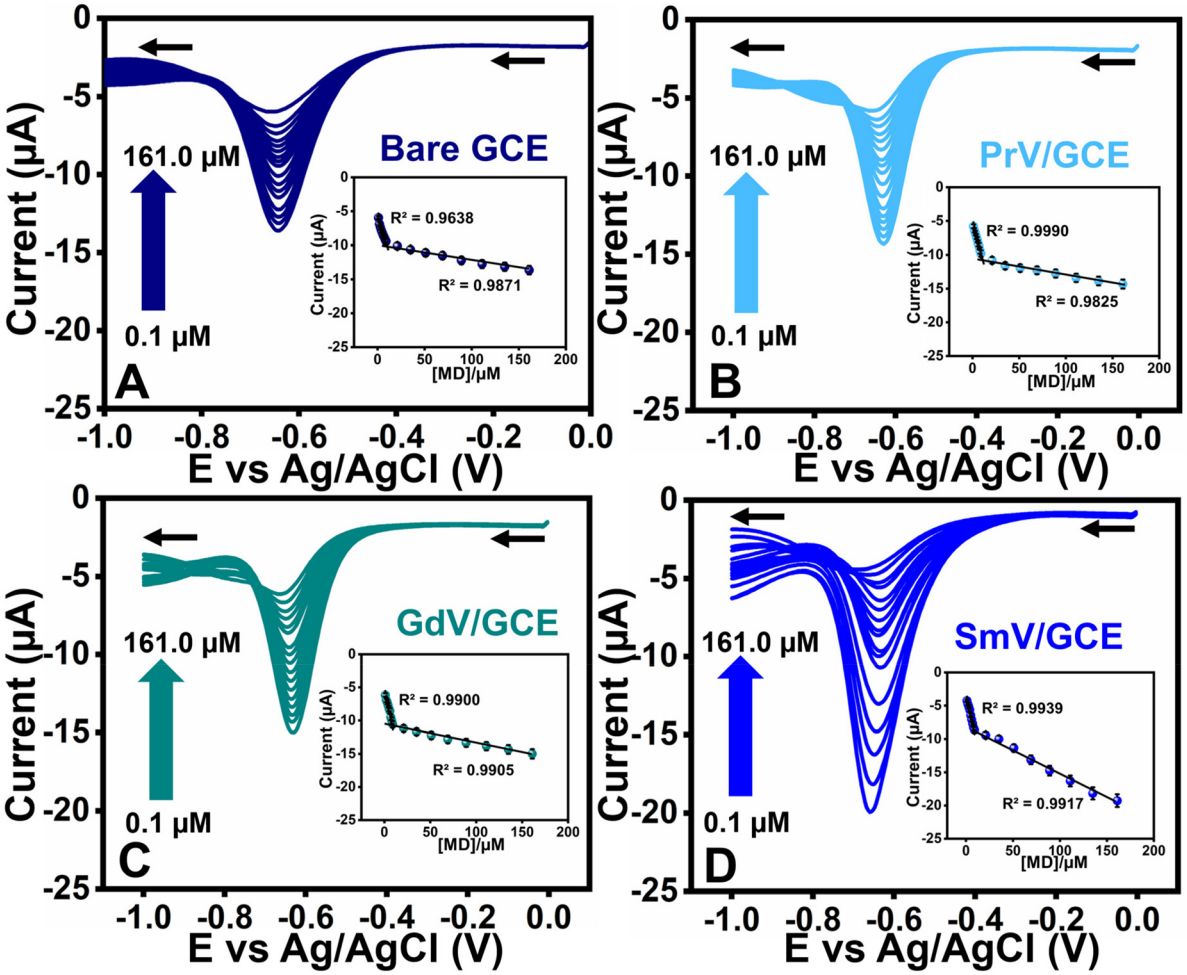

Fig. 8 DPV response of (A) bare GCE, (B) PrV/GCE, (C) GdV/GCE, and (D) SmV/GCE at different concentrations of MD (inset: respective linear plots of concentration *vs.* current).

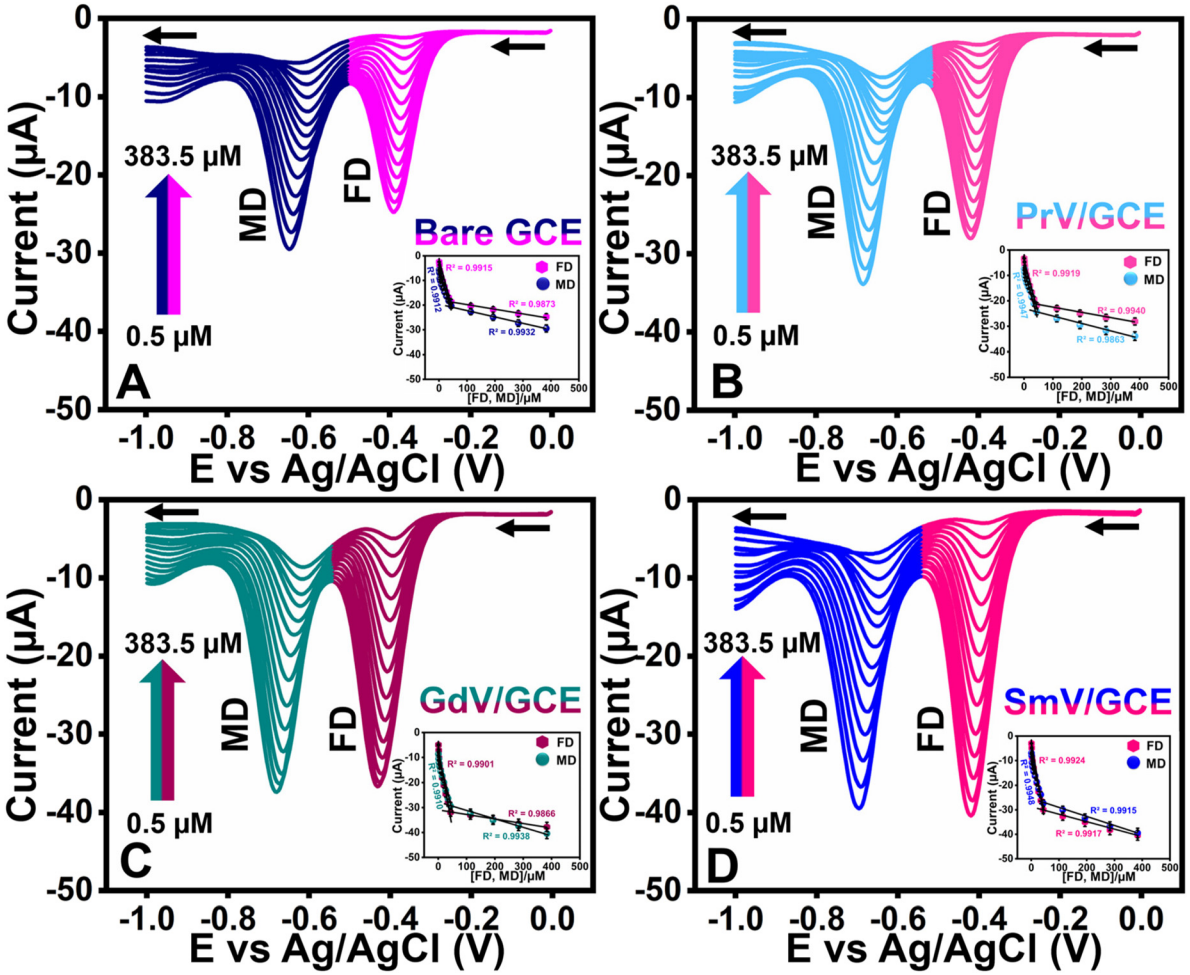

Fig. 9 Simultaneous DPV response of (A) bare GCE, (B) PrV/GCE, (C) GdV/GCE, and (D) SmV/GCE at different concentrations of FD and MD (inset: respective linear plots of concentration *vs.* current).

and lowest LOD (FD = 0.0009 μM and MD = 0.0036 μM) towards FD and MD among all the electrodes.[73,74]

Fig. 9(A–D) present FD and MD simultaneous detection in 0.1 M PBS. The concentration of FD and MD was increased from 0.5–383.5 μM simultaneously for all the electrodes. On increasing the concentration of FD and MD, their respective cathodic peaks also increase gradually and the R^2 values for the electrodes are nearly equal to 1. This indicates the initially reduced products/intermediates from FD/MD do not affect the activity of the modified electrodes upon further increasing the FD and MD concentration, proving the anit-fouling properties of the modified electrodes. The simultaneous DPV results (Fig. 9) resemble the results shown in Fig. 7 and 8. Instead, the LODs for simultaneous results of all the electrodes are slightly increased due to the simultaneous interaction of FD and MD. The LOD for the simultaneous detection of FD and MD in the decreasing order is as follows: Bare-GCE (FD = 0.7782 μM and MD = 1.1106 μM) > PrV/GCE (FD = 0.0191 μM and MD = 0.0465 μM) > GDV/GCE (FD = 0.0116 μM and MD = 0.0201 μM) > SmV/GCE (FD = 0.0015 μM and MD = 0.0049 μM). However, it still shows appreciable LOD and a wide linear range compared to a few already reported literature. Since composite materials will exhibit a low LOD, the lowest LOD could be achieved in the future when making composites with as-synthesized vanadates. Table S5† summarizes the DPV results for the determination of FD and MD. Tables S6 and S7† compare this work's results with previously reported literature for the detection of FD and MD, respectively.

3.8. Interference, cycling stability, repeatability, and reproducibility studies

Fig. S5A† shows that DPV evaluates the anti-interfering ability of the proposed sensor in 0.1 M PBS. Based on already reported literature, the possible interfering compounds for FD and MD, such as a few nitro compounds, biomolecules, and metal ions (possibly present in the real sample), are used as co-interfering interferons. 4-Nitrophenol, fenitrothion, 4-nitroaniline, nitrobenzene, dopamine, uric acid, ascorbic acid, Fe^{2+}, and Na^{+} are used with one-fold higher (200 μM interferons) than FD and MD. Nitro compounds significantly affect the anodic peak currents with a potential shift compared to biomolecules and metal ions. However, the maximum

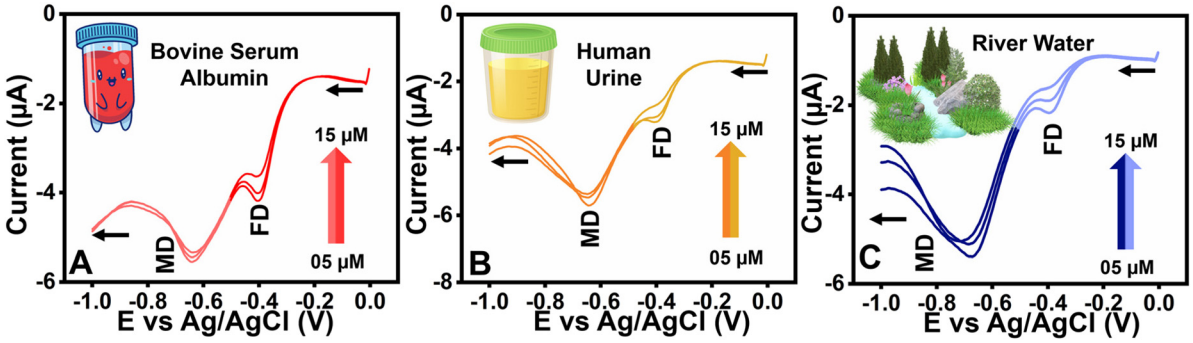

Fig. 10 Real-sample analysis of (A) BSA, (B) human urine, and (C) river water.

current was retained in the end, and the RSD (eqn (6)) shows 3.0% for FD and 1.9% for MD. This shows the appreciable anti-interference ability of the SmV/GCE. The potential cycling stability of the SmV/GCE was calculated by CV in 0.1 M PBS with FD and MD. As shown in Fig. S5B,† the SmV/GCE shows a maximum current retention (eqn (7)) of 86.8% for FD and 87.5% for MD over 50 segments. Furthermore, Fig. S5C and D† show that the SmV/GCE repeatability and reproducibility were determined by DPV in 0.1 M PBS with FD and MD. The repeatability was performed at 4 different times, whereas the reproducibility was determined with 4 different electrodes under the same conditions. The RSD shows good repeatability (FD = 1.4% and MD = 1.0%) and reproducibility (FD = 1.5% and MD = 0.9%) of the SmV/GCE.

3.9. Real-sample analysis of spiked samples

The DPV technique evaluates the real-time sensing capability of SmV/GCE. The applied DPV parameters are: applied potential – 0 to −1.0 V; sensitivity – 1×10^{-005}; pulse period – 0.5 s and amplitude – 0.05 V. Human urine and bovine serum albumin (BSA) are used as real samples. The human urine was collected from a healthy volunteer at the National Taipei University of Technology and the water sample was collected from the Xindian river in Taiwan. Human serum albumin and BSA exhibit chemical similarities due to their encoding *via* the ALB gene. The urine and river water samples were centrifuged at 9000 rpm for 20 min. The obtained supernatant solution was transferred to a separated volumetric flask, and an equal amount of FD and MD was spiked into the urine sample. At the same time, the BSA was purchased from Sigma-Aldrich and used without purification. To prepare the BSA real sample, BSA was dispersed in 0.1 M neutral PBS and stirred to get a homogeneous solution. Similarly, a known amount of FD and MD were spiked into a prepared BSA solution.[75] The standard addition method was followed for the real sample analysis. Fig. 10(A–C) depicts the DPV results of urine and BSA real sample analysis. On the other hand, the concentration of spiked samples increased significantly, and the anodic peak current increased significantly. The SmV/GCE shows a considerable recovery range of 97.40–99.50% (BSA), 98.33–99.20% (human urine), and 97.33–99.70% (river water) towards the FD in real samples. Similarly, 98.00–99.40% (BSA), 97.00–99.30% (human urine), and 98.40–99.60% (river water) of the recovery range were obtained towards MD in real samples. Tables S8 and S9† show the obtained recovery percentage of FD and MD in real samples.

4. Conclusions

A hydrothermal method was employed for the synthesis of REM-VO_4 (REM = Pr, Gd, and Sm). As-synthesized REM-VO_4 differed in their morphology and particle size. The electrochemical reduction behavior of FD and MD was influenced by the respective morphology and particle size of $PrVO_4$, $GdVO_4$, and $SmVO_4$. The improved catalytic behavior of the as-synthesized $SmVO_4$ was attributed to the distinct hollow nature and nanoparticle size. The SmV/GCE exhibits appreciable anti-interference ability, repeatability, and reproducibility where the respective RSDs are less than 5%. The SmV/GCE shows a significant FD and MD recovery range in urine and BSA samples. The obtained LOD values prove that the SmV/GCE could act as an efficient electrochemical tool for the detection of FD and MD individually and simultaneously. To explore the potential utilization for further detection of FD and MD, surface modification of $SmVO_4$ using silane coupling agents could be an effective method to achieve the lowest LOD. The surface modification of $PrVO_4$, $GdVO_4$, and $SmVO_4$ with a silane coupling agent is the potential way to further increase the rate of detection of FD and MD in the future. The silane agent could act as a linker between the catalyst and the target analyte and improve the catalytic behavior to achieve a better LOD.

Abbreviations

FD	Furazolidone
MD	Metronidazole
CV	Cyclic voltammetry
DPV	Differential pulse voltammetry
LSV	Linear sweep voltammetry
i–t	Amperometry

GCE	Glassy carbon electrode
REM	Rare earth metal
EIS	Electrochemical impedance spectroscopy
XRD	X-ray diffraction spectroscopy
FT-IR	Fourier transform Infrared spectroscopy
XPS	X-ray photoelectron spectroscopy
TEM	Transmission electron microscopy
SAED	Selected area electron diffraction
GOF	Goodness of fit
EDX	Energy dispersive X-ray
ACS	Average crystallite size
EASA	Electrochemically active surface area
LOD	Limit of detection
RSD	Relative standard deviation
BSA	Bovine serum albumin

Data availability

The data supporting this article have been included as part of the ESI.†

Conflicts of interest

There are no conflicts to declare.

Acknowledgements

This work was supported by the Ministry of Science and Technology (MOST-108-2221-E-027-063) and the National Taipei University of Technology (NTUT) through their financial support.

References

1 C. Dobell, *Proc. R. Soc. Med.*, 1920, **13**, 1–15.
2 C. A. Kofoid and E. B. Christiansen, *Univ. Calif. Publ. Zool.*, 1915, **16**.
3 K. Muhsen and M. M. Levine, *Clin. Infect. Dis.*, 2012, **55**, S271–S293.
4 M. Dormond, R. L. Gutierrez and C. K. Porter, *Trop. Dis. Travel Med. Vaccines*, 2016, **2**, 1–6.
5 N. R. Salama, M. L. Hartung and A. Müller, *Nat. Rev. Microbiol.*, 2013, **11**, 385–399.
6 D. Y. Graham, *World J. Gastroenterol.*, 2014, **20**, 5191.
7 R. D. Adam, *Clin. Microbiol. Rev.*, 2001, **14**, 447–475.
8 L. L. Lu, T. J. Suscovich, S. M. Fortune and G. Alter, *Nat. Rev. Immunol.*, 2018, **18**, 46–61.
9 R. Malekzadeh, R. Ansari, H. Vahedi, F. Siavoshi, B. Z. Alizadeh, M. R. Eshraghian, A. Vakili, M. Saghari and S. Massarrat, *Aliment. Pharmacol. Ther.*, 2000, **14**, 299–303.
10 B. K. Garg, *Indian J. Pediatr.*, 1972, **39**, 264–266.
11 B.-S. He and G.-A. Du, *Anal. Methods*, 2017, **9**, 4341–4348.
12 Y. Li, Y. Liu, Y. Yang, F. Yu, J. Liu, H. Song, J. Liu, H. Tang, B.-C. Ye and Z. Sun, *ACS Appl. Mater. Interfaces*, 2015, **7**, 15474–15480.
13 A. J. J. Amalraj, N. M. Umesh and S.-F. Wang, *J. Mol. Liq.*, 2020, **313**, 113554.
14 L. Zhang, M. Yin, J. Qiu, T. Qiu, Y. Chen, S. Qi, X. Wei, X. Tian and D. Xu, *Biosens. Bioelectron.:X*, 2022, **10**, 100102.
15 C. Han, W. Yi, Z. Li, C. Dong, H. Zhao and M. Liu, *Electrochim. Acta*, 2023, **447**, 142083.
16 A. Zullo, E. Ierardi, C. Hassan and V. De Francesco, *Saudi J Gastroenterol*, 2012, **18**, 11–17.
17 A. S. Sahib, I. H. Mohammed and S. A. Sloo, *J. Intercult. Ethnopharmacol.*, 2014, **3**, 109.
18 X. Niu, X. Bo and L. Guo, *Food Chem.*, 2021, **364**, 130368.
19 X. Liu, M. K. Ghosh, J. Wang, X. Zhong, M. Muddassir, H. Zhao and K. Ghorai, *Polyhedron*, 2024, **255**, 116958.
20 T. Kokulnathan, T.-J. Wang, M. Thangapandian and S. O. Alaswad, *Appl. Clay Sci.*, 2020, **187**, 105483.
21 K. Mariappan, S. Alagarsamy, S.-M. Chen and S. Sakthinathan, *J. Electrochem. Soc.*, 2023, **170**, 037514.
22 S. Gopi and S.-F. Wang, *Microchim. Acta*, 2023, **190**, 423.
23 D. D. Khandagale and S.-F. Wang, *New J. Chem.*, 2023, **47**, 14933–14942.
24 E. Bakker and M. Telting-Diaz, *Anal. Chem.*, 2002, **74**, 2781–2800.
25 F. R. Simões and M. G. Xavier, *Nanoscience and its Applications*, 2017, vol. 1, pp. 155–178.
26 G. Hussain and D. S. Silvester, *Electroanalysis*, 2018, **30**, 75–83.
27 K. Gokulkumar, S.-J. Huang, Y.-Y. Lee, S. Kogularasu and G.-P. Chang-Chien, *ACS Appl. Nano Mater.*, 2024, 13183–13193.
28 J.-H. Jin, C. Kwon, W. Park, S. Kim and S. Jung, *J. Electroanal. Chem.*, 2008, **623**, 142–146.
29 E. Elanthamilan and S.-F. Wang, *Chemosensors*, 2023, **11**, 544.
30 S. Vinoth and S.-F. Wang, *Food Chem.*, 2023, **427**, 136623.
31 E. Elanthamilan and S.-F. Wang, *Food Chem.*, 2024, 139575.
32 X. B. Joseph, S. Kogularasu, S.-F. Wang and J.-K. Sheu, *ACS Appl. Nano Mater.*, 2021, **4**, 12788–12797.
33 W. D. Adane, B. S. Chandravanshi and M. Tessema, *Sens. Bio-Sens. Res.*, 2024, **45**, 100678.
34 K. Pal, N. Asthana, A. A. Aljabali, S. K. Bhardwaj, S. Kralj, A. Penkova, S. Thomas, T. Zaheer and F. Gomes de Souza, *Crit. Rev. Solid State Mater. Sci.*, 2022, **47**, 691–707.
35 S. Meenakshi, S. J. Sophia and K. Pandian, *Mater. Sci. Eng., C*, 2018, **90**, 407–419.
36 M. Abdullah, K. Pal, P. Singh, H. B. Albargi, R. D. Kale, J. S. Algethami, M. Z. Ahmad and M. M. Rahman, *J. Mol. Liq.*, 2024, **406**, 125096.
37 E. Elaiyappillai, S. Kogularasu, S.-M. Chen, M. Akilarasan, C. E. Joshua, P. M. Johnson, M. A. Ali, F. M. Al-Hemaid and M. Elshikh, *Ultrason. Sonochem.*, 2019, **50**, 255–264.
38 S. Sundaram, R. Jayaprakasam, M. Dhandapani, T. Senthil and V. Vijayakumar, *J. Mol. Liq.*, 2017, **243**, 14–21.
39 K. Abhishek, S. Reddy, S. Acharya, B. Lakshmi, K. Deepak, C. Naveen, K. Harish and S. Ramakrishna, *Anal. Methods*, 2022, **14**, 3228–3249.

40 J. N. Baby, B. Sriram, S.-F. Wang and M. George, *J. Hazard. Mater.*, 2021, **408**, 124940.
41 B. Sriram, S. Kogularasu, Y.-F. Hsu, S.-F. Wang and J.-K. Sheu, *Inorg. Chem.*, 2022, **61**, 16370–16379.
42 B. Sriram, S. Kogularasu, S.-F. Wang and G.-P. Chang-Chien, *ACS Appl. Nano Mater.*, 2024, **7**, 17295–17304.
43 R. K. Devi, M. Ganesan, T.-W. Chen, S.-M. Chen, B.-S. Lou, M. A. Ali, F. M. Al-Hemaid and R.-H. Li, *J. Electroanal. Chem.*, 2022, **923**, 116817.
44 S. Maheshwaran, S. Kogularasu, S.-M. Chen, W.-H. Chen, Y.-Y. Lee and G.-P. Chang-Chien, *J. Taiwan Inst. Chem. Eng.*, 2023, **153**, 105233.
45 T. Kokulnathan and S.-M. Chen, *ACS Sustainable Chem. Eng.*, 2019, **7**, 4136–4146.
46 S. M. Babulal, C. Koventhan, S. M. Chen and W. Hung, *Composites, Part B*, 2022, **237**, 109847.
47 B. Sriram, J. N. Baby, S.-F. Wang, Y.-F. Hsu, V. A. Sherlin and M. George, *Inorg. Chem.*, 2021, **60**, 13150–13160.
48 B. Sriram, J. N. Baby, Y.-F. Hsu, S.-F. Wang and M. George, *Chem. Eng. J.*, 2023, **451**, 138694.
49 A. Radha and S.-F. Wang, *Environ. Sci.:Nano*, 2023, **10**, 3122–3135.
50 R. S. S. Sahayaraj, R. Sundaresan, S.-M. Chen, B. Ramachandran and N. Chandrasekar, *Chem. Inorg. Mater*, 2023, **1**, 100006.
51 R. Monsef, M. Ghiyasiyan-Arani, O. Amiri and M. Salavati-Niasari, *Ultrason. Sonochem.*, 2020, **61**, 104822.
52 N. Yadav, K. Gopalaiah, J. Pandey and R. Nagarajan, *Dalton Trans.*, 2023, **52**, 5969–5975.
53 S. Dutta, S. Pal and S. De, *New J. Chem.*, 2018, **42**, 10161–10166.
54 P. Shandilya, D. Mittal, A. Sudhaik, M. Soni, P. Raizada, A. K. Saini and P. Singh, *Sep. Purif. Technol.*, 2019, **210**, 804–816.
55 K. Leeladevi, J. V. Kumar, M. Arunpandian, M. Thiruppathi and E. Nagarajan, *Mater. Sci. Semicond. Process.*, 2021, **123**, 105563.
56 C. M. Brett, *Molecules*, 2022, **27**, 1497.
57 I. J. D. Priscillal and S.-F. Wang, *Environ. Res.*, 2023, **227**, 115794.
58 Y. Koç, U. Morali, S. Erol and H. Avci, *Turk. J. Chem.*, 2021, **45**, 1895–1915.
59 U. A. Sanjeewani and S.-F. Wang, *Sensors*, 2024, **24**, 1808.
60 V. N. Kendre and S.-F. Wang, *J. Electrochem. Soc.*, 2024, **171**, 057506.
61 B. Akila, S. Sakthinathan, T.-W. Chiu, J. N. Baby and M. George, *ACS Appl. Eng. Mater.*, 2024, 1663–1671.
62 Z. Haghparas, Z. Kordrostami, M. Sorouri, M. Rajabzadeh and R. Khalifeh, *Sci. Rep.*, 2021, **11**, 344.
63 J. Veselinovic, S. AlMashtoub, S. Nagella and E. Seker, *Anal. Chem.*, 2020, **92**, 10751–10758.
64 N. F. Atta and M. F. El-Kady, *Talanta*, 2009, **79**, 639–647.
65 A. A. Ensafi, N. Zandi-Atashbar, M. Gorgabi-Khorzoughi and B. Rezaei, *IEEE Sens. J.*, 2019, **19**, 5396–5403.
66 N. T. Anh, N. N. Huyen, N. X. Dinh, N. T. Vinh, N. Van Quy, V. D. Lam and A.-T. Le, *New J. Chem.*, 2022, **46**, 7090–7102.
67 D. T. N. Nga, N. L. N. Trang, V.-T. Hoang, X.-D. Ngo, P. T. Nhung, D. Q. Tri, N. D. Cuong, P. A. Tuan, T. Q. Huy and A.-T. Le, *RSC Adv.*, 2022, **12**, 27855–27867.
68 K. Sakthivel, A. Muthumariappan, S.-M. Chen, Y.-L. Li, T.-W. Chen and M. A. Ali, *Mater. Sci. Eng., C*, 2019, **103**, 109724.
69 M. A. J. Felix, S. S. R. Shanlee, S.-M. Chen, S. Ruspika, R. Balaji, N. Chandrasekar and P. A. Doss, *Anal. Methods*, 2024, **16**, 2857–2868.
70 I. J. D. Priscillal and S.-F. Wang, *Food Chem.*, 2022, **389**, 133119.
71 S. Vinoth and S.-F. Wang, *Microchim. Acta*, 2022, **189**, 205.
72 J. M. George, A. Antony and B. Mathew, *Microchim. Acta*, 2018, **185**, 1–26.
73 J. Zhu, L. Kong, X. Shen, H. Zhou, G. Zhu, Z. Ji, K. Xu and S. A. Shah, *Dalton Trans.*, 2018, **47**, 9724–9732.
74 L. Zhang, J. Li, C. Wang, L. Huang, M. Huang, Y. Wang, X. Tang, P. Zhao, Y. Xie and J. Fei, *Analyst*, 2022, **147**, 5239–5247.
75 J. N. Baby, B. Sriram, Y.-F. Hsu, S.-F. Wang, R. Bartholomew and M. George, *Microchem. J.*, 2022, **183**, 108067.